Communications in Nonlinear Science and Numerical Simulation 111 (2022) 106433

Contents lists available at ScienceDirect

Communications in Nonlinear Science and Numerical Simulation

journal homepage: www.elsevier.com/locate/cnsns

Research paper

Unconditionally energy stable schemes for fluid-based topology optimization

Yibao Li [a], Kunyang Wang [a], Qian Yu [a], Qing Xia [a], Junseok Kim [b,*]

[a] School of Mathematics and Statistics, Xi'an Jiaotong University, Xi'an 710049, China
[b] Department of Mathematics, Korea University, Seoul 02841, Republic of Korea

ARTICLE INFO

Article history:
Received 17 June 2021
Received in revised form 14 March 2022
Accepted 21 March 2022
Available online 25 March 2022

Keywords:
Phase-field methods
Topology optimization
Stokes equation
Unconditionally energy stable

ABSTRACT

We present first- and second-order unconditionally energy stable schemes for fluid-based topology optimization problems. Our objective functional composes of five terms including mechanical property, Ginzburg–Landau energy, two penalized terms for solid, and the volume constraint. We consider the steady-state Stokes equation in the fluid domain and Darcy flow through porous medium. By coupling a Stokes type equation and the Allen–Cahn equation, we obtain the evolutionary equation for the fluid-based topology optimization. We use the backward Euler method and the Crank–Nicolson method to discretize the coupling system. The first- and second-order accurate schemes are presented correspondingly. We prove that our proposed schemes are unconditionally energy stable. The preconditioned conjugate gradient method is applied to solve the system. Several numerical tests are performed to verify the efficiency and accuracy of our schemes.

1. Introduction

Topological optimization for Stokes flow has been applied to many fields such as fluid flow, species transport, heat transfer and mechanical engineering [1–9]. Up to now, a great number of methods have been proposed to solve topology optimization problem of fluid, including the explicit boundary methods [10,11], surface-capturing methods [12–15] and density-based methods [16–19]. The explicit boundary method is based on a classical physics. However, fully re-meshing and regularization of the interface may pose difficulties in computing. For surface-capturing methods, the interface can easily couple different physics because of its well-defined and crisp interface. The density-based method recently has become more and more popular [20–22]. The phase field method has been developed as a way to describe phase transition phenomena such as solid–liquid transitions [23,24]. In this method, the thin transition region replaces the sharp interface and smooth continuous variable is introduced to locate phase or grains boundaries avoiding the explicit front tracking.

Duan et al. [25] considered topology optimization of two immiscible fluids. They combined a diffuse interface model with the level set method to implement their proposed method. Coffin and Maute [26] used the level set method to describe the geometric shape and used the extended finite element method (XFEM) to predict the temperature field. By introducing a spatial gradient constraint of the level set field, they solved the topology optimization of convective heat transfer problems in two and three dimensions. Li et al. [27] applied the phase field method to fluid-based shape optimization and used FEM to solve this problem. Instead of using fixed meshes globally, the locally refined mesh

* Corresponding author.
E-mail addresses: yibaoli@xjtu.edu.cn (Y. Li), cfdkim@korea.ac.kr (J. Kim).
URLs: http://gr.xjtu.edu.cn/web/yibaoli (Y. Li), https://mathematicians.korea.ac.kr/cfdkim (J. Kim).

https://doi.org/10.1016/j.cnsns.2022.106433
1007-5704/

near the interface was used, which had advantages of low computational expense. In the previous studies, the energy stability [28–31] of their schemes were not proved. Chen et al. [32] proposed a topology optimization for fluids with the Stokes equation by using an efficient threshold dynamics method. They solved this problem by the iterative scheme in which they had proved the total energy decaying property. These existing works include the first-order [33], the second-order [34], and the third-order energy stable linear schemes [35] for the thin film equations without slope selection. Stabilization and regularization terms have been extensively studied. Yang and Kim developed an unconditionally stable linear numerical scheme for the N-component Cahn–Hilliard system with second-order accuracy in time and space [36]. In our previous paper, we proposed the phase field method to deal with the compliance minimization problem in topology optimization [37]. The developed equation coupled the diffusive interface dynamics and the linear elasticity solid mechanics. The energy stability and convergence analysis have been theoretically justified.

In this paper, we use the linear energy stability for the fluid-based topology optimization in the different contexts and applications. We consider the steady-state Stokes equation in the fluid domain and Darcy flow through porous medium, which have been introduced for topology optimization in fluid flow in [38,39]. The objective functional composes of five parts including a term for the fluid mechanical property, Ginzburg–Landau energy, two penalized terms for the solid mechanical property, and one penalized term for the volume constraint. This results in a diffuse interface problem, which approximates a sharp interface problem for topology optimization in fluids that is penalized by four perimeter terms. The diffuse interface model has advantages in describing topological changes in fluid flow [40–42]. We present first- and second-order unconditionally energy stable schemes for fluid-based topology optimization problems. Energy stability has been widely investigated for numerical schemes of classic PDE-based phase field models. The backward Euler and Crank–Nicolson type methods are used to discretize the coupling governing system. We use the preconditioned conjugate gradient method to solve this system. The proofs of the unconditional energy stabilities of the proposed schemes will be given. Several numerical tests will be performed to verify the efficiency and accuracy of the proposed schemes. Topology and shape optimization are sub-fields within structural optimization. Shape optimization methods work in a subset of allowable shapes which have fixed topological properties. Topological optimization method can then help work around the limitations of pure shape optimization. Our method can be used to obtain the topology and shape optimized structures. It should be noted that in [37], we have proposed an efficient method to find the optimal distribution of materials for elasticity. While in this paper, we focus on the fluid-based topology optimization method. The different context leads to significantly different governing equation and numerical scheme. The main contributions can be summarized as the following:

- We present first-order and second-order unconditionally energy stable schemes for fluid-based topology optimization problem.
- We prove the unconditional energy stabilities of the proposed two schemes. Therefore, we can use a larger time step and obtain the convergent solution of the original topology optimization problem.
- The proposed method is simple and easy to implement because only two Poisson-type equations and one heat-type equation need to be solved.

The paper is organized as follows. In Section 2, we formulate the model for fluid-based topology optimization using phase field method. The proposed numerical schemes and their proofs of unconditional energy stability are shown in Section 3. In Section 4, several numerical results are presented. The conclusion is given in Section 5.

2. Topology optimization for Stokes flow

In this section, a mathematical model for topology optimization of fluids in Stokes flow is considered. The computational domain is denoted by $\Omega \in \mathbb{R}^d (d = 2, 3)$ and the outer normal vector for Ω is denoted by $\mathbf{n}$. For any $\mathbf{x} \in \Omega$, the order parameter $\phi(\mathbf{x})$ is a function of bounded variation in Ω. Here, $\phi(\mathbf{x})$ is defined by $\phi(\mathbf{x}) = 1$ in the solid region $\Omega \backslash \Omega_0$ and $\phi(\mathbf{x}) = 0$ in the fluid region $\Omega_0 \subset \Omega$. The basic problem of topology optimization is to determine an optimal shape of Ω_0 which minimize the following objective functional consisting of the total potential power and a perimeter regularization term:

$$\min_{(\phi,\mathbf{u})} J_0(\phi, \boldsymbol{u}) = \int_\Omega \Big(\frac{\mu}{2} |\nabla \boldsymbol{u}|^2 - \boldsymbol{f} \cdot \boldsymbol{u} \Big) d\mathbf{x} + \gamma \Gamma(\Omega_0), \tag{2.1}$$

which subjects to

$$\phi = 1 \text{ or } \phi = 0 \quad \text{in } \Omega, \tag{2.2}$$

and

$$\nabla p - \nabla \cdot (\mu \nabla \mathbf{u}) = \mathbf{f} \quad \text{in } \Omega_0, \tag{2.3}$$

$$\nabla \cdot \mathbf{u} = 0 \quad \text{in } \Omega, \tag{2.4}$$

$$\mathbf{u} = \mathbf{0} \quad \text{in } \Omega \backslash \Omega_0, \tag{2.5}$$

$$\mathbf{f} = \mathbf{0} \quad \text{in } \Omega \backslash \Omega_0, \tag{2.6}$$

$$\begin{aligned} \mathbf{n}\cdot\nabla p &= 0 \quad \text{on } \partial\Omega, \\ \mathbf{u} &= \mathbf{g} \quad \text{on } \partial\Omega, \\ \int_\Omega \phi \mathrm{d}\mathbf{x} &= V_0, \end{aligned} \tag{2.7}$$

where $\Gamma(\Omega_0)$ represents the perimeter term of Ω_0. $\mathbf{u}$ denotes the velocity of the fluid, $\nabla\mathbf{u}$ is the distributional derivative of $\mathbf{u}$, p is the pressure, $\mu > 0$ represents the viscosity of the fluid, $\boldsymbol{f}$ represents external forces loaded on the domain Ω. It should be noted that the velocity of the fluid is defined not only on the fluid region Ω_0, but rather on the whole of Ω, because the velocity is determined by the stationary Stokes equation (Eq. (2.3)) in Ω_0, and on the remainder we set the velocity equal to zero (Eq. (2.5)). Therefore, the force $\boldsymbol{f}$ and velocity $\mathbf{u}$ are defined in the whole domain Ω. V_0 is the volume of the solid region and $\gamma > 0$ is a weighting parameter. In addition, the objective functional $\int_\Omega \left(\frac{\mu}{2}|\nabla\boldsymbol{u}|^2 - \boldsymbol{f}\cdot\boldsymbol{u}\right)d\mathbf{x}$ describes the total potential power. Because $\Omega_0 := \{\phi = 0\}$, Eq. (2.7) can be rewritten as $\int_\Omega \phi \mathrm{d}\mathbf{x} = \int_{\Omega\setminus\Omega_0} \phi \mathrm{d}\mathbf{x} = V_0$. For a more detailed introduction to the theory of Caccioppoli sets and the perimeter term, please refer to [43]. For simplicity of exposition, Dirichlet boundary condition $\mathbf{u} = \mathbf{g}$ is applied on $\partial\Omega$. Note that our method can also be extended to cases involving periodic and Neumann boundary conditions. In the objective functional (Eq. (2.1)), we replace the perimeter functional $\Gamma(\Omega_0)$ by the Ginzburg–Landau energy, which is defined as:

$$E(\phi) = \int_\Omega \left(\frac{\varepsilon}{2}|\nabla\phi|^2 + \frac{1}{\varepsilon}F(\phi)\right)d\mathbf{x}, \tag{2.8}$$

where $F(\phi) = \phi^2(1-\phi)^2/4$, $\varepsilon > 0$ is the interfacial thickness between fluid and non-fluid regions. Then, the hyper surface between fluid and nonfluid regions is replaced by an interfacial layer with thickness proportional to the small parameter ε, the design variable ϕ is allowed to have values in [0, 1] instead of only 0 or 1. From a constrained gradient flow of the free energy functional (2.8), we can derive the Allen–Cahn equation, which has been applied in various applications [37,44–51]. In order to ensure vanishing of the velocity outside the fluid domain, we add the penalty term $\int_\Omega \alpha(\phi)|\mathbf{u}|^2/2d\mathbf{x}$ to the objective function. Here, $\alpha(\phi) : [0,1] \to [0, \alpha_\varepsilon]$ is a smooth function of ϕ and α_ε is a large positive constant. When $\alpha(\phi) = 0$, one retains Stokes flow and when $\alpha(\phi) = \alpha_\varepsilon$, one gets the Darcy equation that governs porous media flow. This porous medium approach has been introduced for topology optimization in fluid flow by [39]. We choose $\alpha(\phi)$ as following:

$$\alpha(\phi) = \alpha_\varepsilon\phi. \tag{2.9}$$

Let $\Omega_1 \subset \Omega\setminus\Omega_0$ be a fixed solid area and we define a new function $\psi(\mathbf{x})$ as

$$\psi(\mathbf{x}) := \begin{cases} 1 & \text{if } \mathbf{x} \in \Omega_1, \\ 0 & \text{if } \mathbf{x} \in \Omega\setminus\Omega_1. \end{cases} \tag{2.10}$$

To keep the design variable ϕ in the fixed solid area to be almost the same as those in the originally known value ψ, we use a fidelity term $\int_\Omega \overline{\lambda}(\phi-\psi)^2/2d\mathbf{x}$. For this purpose, $\overline{\lambda} = \lambda$ if $\mathbf{x} \in \Omega_1$; otherwise $\overline{\lambda} = 0$. Here, λ is a positive constant. We use a penalization term to ensure the volume of solid $A(\phi) := \int_\Omega \phi\, d\mathbf{x}$ be V_0 and arrive at an additional penalization term $\beta(A(\phi)-V_0)^2/2$. Here, β is a positive constant. Finally, our objective functional is proposed as follows:

$$\begin{aligned} \min_{(\phi,\mathbf{u})} J(\phi,\mathbf{u}) = &\int_\Omega \left(\frac{\mu}{2}|\nabla\mathbf{u}|^2 - \mathbf{u}\cdot\mathbf{f}\right)d\mathbf{x} + \gamma\int_\Omega \left(\frac{\varepsilon}{2}|\nabla\phi|^2 + \frac{1}{\varepsilon}F(\phi)\right)d\mathbf{x} + \int_\Omega \frac{\alpha(\phi)}{2}|\mathbf{u}|^2 d\mathbf{x} \\ &+ \int_\Omega \frac{\overline{\lambda}}{2}(\phi-\psi)^2 d\mathbf{x} + \frac{\beta}{2}(A(\phi)-V_0)^2, \end{aligned} \tag{2.11}$$

which subjects to $\phi \in [0,1]$ and

$$\nabla p - \nabla\cdot(\mu\nabla\mathbf{u}) + \alpha(\phi)\mathbf{u} = \mathbf{f} \quad \text{in } \Omega, \tag{2.12}$$

$$\nabla\cdot\mathbf{u} = 0 \quad \text{in } \Omega, \tag{2.13}$$

$$\mathbf{n}\cdot\nabla p = 0 \quad \text{on } \partial\Omega, \tag{2.14}$$

$$\mathbf{u} = \mathbf{g} \quad \text{on } \partial\Omega. \tag{2.15}$$

It should be noted that by adding the term $\alpha_\varepsilon\phi$ to Eq. (2.3), Eq. (2.12) is the interpolation between the steady-state Stokes equation in the fluid domain and Darcy flow through porous medium at the solid domain. Therefore α_ε should not be zero. In fact, we have weaken the condition of non-permeability through the solid region by introducing a diffuse interface approximation. Note that to ensure that the velocity vanishes outside the fluid region in the limit $\epsilon \to 0$, we have added an additional penalization term to the objective functional in Eq. (2.11). This porous medium approach has been introduced for topology optimization in fluid flow in [38,39]. To ensure $A(\phi)$ to be V_0, we have added a fidelity term to Eq. (2.11). To keep the design variable ϕ in the fixed solid area to be almost the same as those in the originally known value ψ, we have used a fidelity term $\int_\Omega \overline{\lambda}(\phi-\psi)^2/2d\mathbf{x}$.

Now, we review the derivation of the proposed equation. By introducing an artificial time variable t, we aim to find a stationary order parameter ϕ in the following gradient flow:

$$\frac{\partial \phi}{\partial t} = -\frac{\delta J}{\delta \phi}. \tag{2.16}$$

Here, the chemical potential $\delta J/\delta\phi$ is obtained via the variational derivative of the objective functional (2.11) with respect to ϕ, i.e.,

$$\begin{aligned}
&\left(\frac{\delta J}{\delta \phi}, v\right)_{L_2} = \left.\frac{d}{d\eta} J(\phi + \eta v, \mathbf{u})\right|_{\eta=0} \\
&= \frac{\gamma}{\varepsilon}\int_\Omega \left(vF'(\phi) + \varepsilon^2 \nabla v \cdot \nabla \phi\right) d\mathbf{x} - \int_\Omega v(\bar{\lambda}(\phi-\psi) + \frac{\alpha'(\phi)}{2}|\mathbf{u}|^2 + \beta\,(A(\phi)-V_0))d\mathbf{x} \\
&= \frac{\gamma}{\varepsilon}\int_\Omega \left(F'(\phi) - \varepsilon^2 \Delta\phi\right) v d\mathbf{x} - \int_\Omega v(\bar{\lambda}(\phi-\psi) + \frac{\alpha'(\phi)}{2}|\mathbf{u}|^2 + \beta\,(A(\phi)-V_0))d\mathbf{x} + \gamma\int_{\partial\Omega} \varepsilon^2 \frac{\partial\phi}{\partial n} v ds \\
&= \int_\Omega \left(\frac{\gamma}{\varepsilon}F'(\phi) - \frac{\gamma}{\varepsilon}\varepsilon^2\Delta\phi - \bar{\lambda}(\phi-\psi) - \frac{\alpha'(\phi)}{2}|\mathbf{u}|^2 - \beta\,(A(\phi)-V_0)\right) v d\mathbf{x},
\end{aligned} \tag{2.17}$$

where $(,)_{L_2}$ is L_2 norm inner product and the Neumann boundary condition for ϕ, i.e., $\mathbf{n}\cdot\nabla\phi = 0$, is assumed. Thus,

$$\frac{\delta J}{\delta \phi} = \frac{\gamma}{\varepsilon}F'(\phi) - \gamma\varepsilon\Delta\phi + \bar{\lambda}(\phi-\psi) + \frac{\alpha'(\phi)}{2}|\mathbf{u}|^2 + \beta\,(A(\phi)-V_0)\,. \tag{2.18}$$

Substituting Eq. (2.18) into Eq. (2.16) yields

$$\frac{\partial \phi}{\partial t} = -\frac{\gamma}{\varepsilon}F'(\phi) + \gamma\varepsilon\Delta\phi - \bar{\lambda}(\phi-\psi) - \frac{\alpha'(\phi)}{2}|\mathbf{u}|^2 - \beta(A(\phi)-V_0). \tag{2.19}$$

In addition, the derivation of the proposed equation for the velocity $\mathbf{u}$ in a gradient flow is reviewed:

$$\begin{aligned}
&\left(\frac{\delta J}{\delta \mathbf{u}}, \mathbf{w}\right)_{L_2} = \left.\frac{d}{d\eta} J(\phi, \mathbf{u} + \eta\mathbf{w})\right|_{\eta=0} \\
&= \int_\Omega (\mu\nabla\mathbf{u}\cdot\mathbf{w})\,d\mathbf{x} - \int_\Omega \mathbf{f}\cdot\mathbf{w}d\mathbf{x} + \int_\Omega \alpha(\phi)\mathbf{u}\cdot\mathbf{w}d\mathbf{x} - \int_\Omega p\nabla\cdot\mathbf{w}d\mathbf{x} - \int_{\partial\Omega}(\mathbf{u}-\mathbf{g})\mathbf{w}d\mathbf{s} - \int_{\partial\Omega}\mathbf{n}\cdot\nabla p d\mathbf{s} \\
&= \int_\Omega \Big(\alpha(\phi)\mathbf{u} + \nabla p - \nabla\cdot(\mu\nabla\mathbf{u}) - \mathbf{f}\Big)\mathbf{w}d\mathbf{x},
\end{aligned} \tag{2.20}$$

where we have used Eqs. (2.13)–(2.15). Thus, we obtain

$$\frac{\delta J}{\delta \mathbf{u}} = \nabla p - \nabla\cdot(\mu\nabla\mathbf{u}) + \alpha(\phi)\mathbf{u} - \mathbf{f}. \tag{2.21}$$

Substituting Eq. (2.21) into Eq. (2.12) yields

$$\frac{\delta J}{\delta \mathbf{u}} = \nabla p - \nabla\cdot(\mu\nabla\mathbf{u}) + \alpha(\phi)\mathbf{u} - \mathbf{f} = 0. \tag{2.22}$$

By using the gradient flow method, we can accurately capture the trajectory leading to the solution of Eq. (2.19). Under appropriate assumptions, Garcke et al. proved the existence of minimizers to the classical phase field optimization problem and derived the first order optimality condition [52,53]. While the difficulty lies in establishing the general existence of Eq. (2.19) because of the associated Lagrange multipliers. We will not consider the existence proof of Eq. (2.19) in this context. There exist unique solutions $\mathbf{u}$ and p of Eqs. (2.12) and (2.13). The existence proof can be obtained by using the theory of pseudo monotone operators and the uniqueness statement of stationary Stoke equations [54–56]. For details on the existence proof of the unique solution $\mathbf{u}$ and how to include the pressure in the objective functional (Eq. (2.12)), we refer the reader to [57]. Considering the state Eqs. (2.12) and (2.19), we find the following solvability result.

Theorem 2.1. *The solutions $\mathbf{u}$, p, and ϕ of Eqs. (2.12), (2.13), and (2.19) possess the property that the total energy $J(\phi,\mathbf{u})$ decreases with time, i.e., $dJ/dt \le 0$.*

Proof.

$$\begin{aligned}
\frac{dJ}{dt} &= \int_\Omega \Big(\mu\nabla\mathbf{u}\cdot\nabla\mathbf{u}_t - \mathbf{f}\cdot\mathbf{u}_t\Big)d\mathbf{x} + \gamma\int_\Omega\Big(\frac{1}{\varepsilon}F'(\phi)\cdot\phi_t - \varepsilon\Delta\phi\cdot\phi_t\Big)d\mathbf{x} \\
&\quad + \int_\Omega\Big(\alpha(\phi)\mathbf{u}\cdot\mathbf{u}_t + \frac{1}{2}\alpha'(\phi)|\mathbf{u}|^2\cdot\phi_t\Big)d\mathbf{x} + \int_\Omega \bar{\lambda}(\phi-\psi)\cdot\phi_t d\mathbf{x} + \int_\Omega \beta(A(\phi)-V_0)\cdot\phi_t d\mathbf{x}.
\end{aligned} \tag{2.23}$$

By taking the inner product of Eq. (2.12) with $\mathbf{u}_t$, we obtain

$$\int_\Omega \Big(\nabla p\cdot\mathbf{u}_t-\big(\nabla\cdot(\mu\nabla\mathbf{u})\big)\cdot\mathbf{u}_t+\alpha(\phi)\mathbf{u}\cdot\mathbf{u}_t\Big)d\mathbf{x}=\int_\Omega \mathbf{f}\cdot\mathbf{u}_t d\mathbf{x}, \tag{2.24}$$

$$\int_\Omega \mu\nabla\mathbf{u}\cdot\nabla\mathbf{u}_t+\alpha(\phi)\mathbf{u}\cdot\mathbf{u}_t-\mathbf{f}\cdot\mathbf{u}_t d\mathbf{x}=\int_\Omega -\nabla p\cdot\mathbf{u}_t d\mathbf{x}=\int_\Omega p\nabla\cdot\mathbf{u}_t d\mathbf{x}=0. \tag{2.25}$$

By taking the inner product of Eq. (2.19) with $-\phi_t$, we have

$$\int_\Omega \phi_t\cdot(-\phi_t)d\mathbf{x}=\int_\Omega\Big(\frac{\gamma}{\varepsilon}F'(\phi)\cdot\phi_t-\gamma\varepsilon\Delta\phi+\bar{\lambda}(\phi-\psi)+\frac{\alpha'(\phi)}{2}|\mathbf{u}|^2+\beta(A(\phi)-V_0)\Big)\cdot\phi_t d\mathbf{x}. \tag{2.26}$$

Combining Eqs. (2.25) and (2.26), we get

$$\frac{dJ}{dt}=-\int_\Omega \phi_t^2 d\mathbf{x}\le 0. \quad \square \tag{2.27}$$

3. Numerical schemes

Let us denote some notations at the beginning. We focus on describing this idea in two-dimensional space. The extension to three-dimensional domains is straightforward. For simplicity, the design domain for our scheme is set as a rectangular domain $\Omega=[0,L_x]\times[0,L_y]$ and $h=L_x/N_x=L_y/N_y$ is defined as uniform mesh size, where N_x and N_y are two positive even integers and $N=N_xN_y$. The staggered marker-and-cell mesh is used. In this mesh, the pressure p and phase fields ϕ are stored at the cell centers, and the velocities $\mathbf{u}(u,v)$ are saved at the cell edges. Let ϕ_{ij}^n be an approximation to $\phi(x_i,y_j,n\Delta t)$, where $x_i=(i-0.5)h$, $y_j=(j-0.5)h$, and Δt is the time step. The cell vertices are located at $(x_{i+\frac12},y_{j+\frac12})=(ih,jh)$. Some discrete operators are defined as follows.

$$\nabla_d\phi_{i,j}=\big(D_x\phi_{i+\frac12,j},D_y\phi_{i,j+\frac12}\big),\quad D_x\phi_{i+\frac12,j}=\frac{\phi_{i+1,j}-\phi_{i,j}}{h},\ D_y\phi_{i,j+\frac12}=\frac{\phi_{i,j+1}-\phi_{i,j}}{h},$$

$$\Delta_d\phi_{i,j}=\frac{\phi_{i-1,j}+\phi_{i+1,j}+\phi_{i,j-1}+\phi_{i,j+1}-4\phi_{i,j}}{h^2},$$

$$(\phi,\psi)_d=h^2\sum_{i=1}^{N_x}\sum_{j=1}^{N_y}\phi_{i,j}\psi_{i,j},\ A_d(\phi)=h^2\sum_{i=1}^{N_x}\sum_{j=1}^{N_y}\phi_{i,j}=(\phi,\mathbf{1})_d.$$

$$(\nabla_d\phi,\nabla_d\psi)_d=h^2\sum_{i=1}^{N_x}\sum_{j=1}^{N_y}\big(D_x\phi_{i+\frac12,j}D_x\psi_{i+\frac12,j}+D_y\phi_{i,j+\frac12}D_y\psi_{i,j+\frac12}\big).$$

$$\|\phi\|_d^2=(\phi,\phi)_d,\quad \|\nabla_d\phi\|_d^2=(\nabla_d\phi,\nabla_d\phi)_d.$$

Here, $\mathbf{1}$ is an N_x-by-N_y matrix of ones. One of the desirable properties for the discretized system to have is to maintain its own energy dissipation law that is consistent with the energy law obeyed by the continuous system. Practically, this is an indication for a good approximation to the differential dissipative system [58]. In the following, the first-order and second-order energy stable schemes will be devised for Eqs. (2.12), (2.13), and (2.19). In the first-order scheme, only three decoupled elliptic equations with constant coefficients are solved at each time step, which makes it easy to implement. The second-order scheme is a coupling method but achieves second-order accuracy in time and space. We will show that the proposed two discrete schemes satisfy semi-discrete energy-dissipation law and are therefore unconditionally energy stable.

3.1. The first-order scheme

The first-order linearly stabilized splitting schemes for Eqs. (2.12), (2.13), and (2.19) are given as follows:

$$\frac{\phi^{n+1}-\phi^n}{\Delta t}=-\frac{\gamma}{\varepsilon}F'(\phi^n)-\frac{\gamma\xi}{2\varepsilon}(\phi^{n+1}-\phi^n)+\gamma\varepsilon\Delta_d\phi^{n+1}-\frac{\alpha'(\phi^{n+1})}{2}|\mathbf{u}^n|^2-\bar{\lambda}(\phi^{n+1}-\psi)-\beta\big(A_d(\phi^{n+1})-V_0\big), \tag{3.1}$$

$$\nabla_d p^{n+1}-\nabla_d\cdot(\mu\nabla_d\mathbf{u}^{n+1})+\alpha(\phi^{n+1})\mathbf{u}^{n+1}=\mathbf{f}, \tag{3.2}$$

$$\nabla_d\cdot\mathbf{u}^{n+1}=0, \tag{3.3}$$

A stabilizing term $\frac{\gamma\xi}{2\varepsilon}(\phi^{n+1}-\phi^n)$ is introduced in Eq. (3.1). Here, ξ is a positive parameter. Note that the system (3.1)–(3.3) has the first order accuracy in time and second order accuracy in space. The term $A_d(\phi^{n+1})$ in Eq. (3.1) cannot be solved because of the unknown ϕ^{n+1} in the nth time step. By taking the inner product of Eq. (3.1) with $\mathbf{1}$, we obtain

$$A_d(\phi^{n+1}) = \frac{(\frac{1}{\Delta t}+\frac{\gamma\xi}{2\varepsilon})A_d(\phi^n) + N\beta h^2 V_0 + \sum_{i=1}^{N_x}\sum_{j=1}^{N_y}\left(\bar{\lambda}\psi - \frac{\gamma}{\varepsilon}F'(\phi^n) - \frac{\alpha'(\phi^{n+1})}{2}|\mathbf{u}^n|^2\right)}{\frac{1}{\Delta t}+\frac{\gamma\xi}{2\varepsilon}+\bar{\lambda}+\beta N h^2}. \tag{3.4}$$

Here, $\alpha(\phi)$ is a linear function of ϕ (Eq. (2.9)), then $\alpha'(\phi^{n+1}) = \alpha_\varepsilon$. Therefore, we can replace the original definition of $A_d(\phi^{n+1})$ by Eq. (3.4). Next, we describe the overall procedure for the numerical solution from n to $n+1$ time step. With a given divergence-free velocity field $\mathbf{u}^n$ and an order parameter ϕ^n, we want to find $\mathbf{u}^{n+1}$ and ϕ^{n+1}:

Step 1. Compute $A(\phi^{n+1})$ by Eq. (3.4).

Step 2. Solve Eq. (3.1) by using the preconditioning conjugate gradient method to get ϕ^{n+1} from $\mathbf{u}^n$ and ϕ^n.

Step 3. Solve the Stokes Eqs. (3.2) and (3.3) to get $\mathbf{u}^{n+1}$ and p^{n+1} from $\mathbf{u}^n$ and p^n.

By taking the divergence on both sides of Eq. (3.2) and using the incompressible condition Eq. (3.3), we obtain

$$\Delta_d p^{n+1} + \nabla_d\cdot(\alpha(\phi^{n+1})\mathbf{u}^{n+1}) = \nabla_d\cdot\mathbf{f}. \tag{3.5}$$

Then, Eqs. (3.2) and (3.5) are transformed into a linear system of $\mathbf{u}^{n+1}$ and p^{n+1}, which can be solved with a preconditioned conjugate gradient method. This completes the process (Step 1–Step 3) by which the variables $\mathbf{u}^{n+1}$, p^{n+1}, and ϕ^{n+1} are calculated. Because Eq. (3.1) is linear equation of ϕ^{n+1} and Eqs. (3.2) and (3.5) are a linear system of $\mathbf{u}^{n+1}$ and p^{n+1}, existence follows from uniqueness for our first-order scheme. As in the semi-discrete case, the discrete total energy is defined as

$$\begin{aligned} J(\phi^{n+1},\mathbf{u}^{n+1}) &= \frac{\mu}{2}\left(\nabla_d\mathbf{u}^{n+1},\nabla_d\mathbf{u}^{n+1}\right)_d - \left(\mathbf{u}^{n+1},\mathbf{f}\right)_d + \frac{\gamma}{\varepsilon}\left(F(\phi^{n+1}),1\right)_d + \frac{\gamma\varepsilon}{2}\left(\nabla_d\phi^{n+1},\nabla_d\phi^{n+1}\right)_d \\ &+ \frac{1}{2}\left(\alpha(\phi^{n+1})\mathbf{u}^{n+1},\mathbf{u}^{n+1}\right)_d + \frac{\bar{\lambda}}{2}\left(\phi^{n+1}-\psi,\phi^{n+1}-\psi\right)_d + \frac{\beta}{2}\left(A_d(\phi^{n+1})-V_0,A_d(\phi^{n+1})-V_0\right)_d. \end{aligned} \tag{3.6}$$

Remark 1. In this work, we restrict our attention to the order parameter ϕ which is bounded such that $\phi \le \mathcal{M}$. It is well known that the original Allen–Cahn equation satisfies the maximum principle [59–63]. Eq. (2.19), which is a modified Allen–Cahn equation, may satisfy the maximum principle, because this condition can be satisfied by many physically relevant potentials by restricting the growth of $F(\phi)$ to be quadratic for $\phi \ge \mathcal{M}$. It is very difficult to analytically prove that the solution for Eq. (2.19) is bounded because $F(\phi)$ exhibits quartic growth at infinity and the velocity $\mathbf{u}$ is coupled to the order parameter ϕ. Based on our numerical experiment, we can find that the solution for Eq. (2.19) with the original double-well potential is bounded if the maximum norm of initial condition $\phi^0 \in [0,1]$ is bounded. Therefore, M may be non-significantly larger than 1.

Now, we will prove the unconditional energy stability $J(\phi^{n+1},\mathbf{u}^{n+1}) \le J(\phi^n,\mathbf{u}^n)$ under the condition $\xi \ge F''(\mathcal{M})$.

Lemma 3.1. *Under the condition that $\xi \ge F''(\mathcal{M})$, the solutions $(\phi^{n+1},\phi^n,\mathbf{u}^n)$ of the scheme (3.1) satisfy*

$J(\phi^{n+1},\mathbf{u}^n) \le J(\phi^n,\mathbf{u}^n)$.

Proof. By taking inner product of Eq. (3.1) with $-(\phi^{n+1}-\phi^n)$, we get

$$-\left(\frac{\phi^{n+1}-\phi^n}{\Delta t},\phi^{n+1}-\phi^n\right)_d = -\frac{1}{\Delta t}\|\phi^{n+1}-\phi^n\|_d^2. \tag{3.7}$$

$$\left(\frac{\gamma\xi}{2\varepsilon}(\phi^{n+1}-\phi^n),\phi^{n+1}-\phi^n\right)_d = \frac{\gamma\xi}{2\varepsilon}\|\phi^{n+1}-\phi^n\|_d^2. \tag{3.8}$$

$$\begin{aligned} -(\gamma\varepsilon\Delta_d\phi^{n+1},\phi^{n+1}-\phi^n)_d &= \gamma\varepsilon\left(\nabla_d\phi^{n+1},\nabla_d\phi^{n+1}-\nabla_d\phi^n\right)_d \\ &= \frac{\gamma\varepsilon}{2}\left(\|\nabla_d\phi^{n+1}\|_d^2 - \|\nabla_d\phi^n\|_d^2 + \|\nabla_d\phi^{n+1}-\nabla_d\phi^n\|_d^2\right). \end{aligned} \tag{3.9}$$

$$\left(\bar{\lambda}(\phi^{n+1}-\psi),\phi^{n+1}-\phi^n\right)_d = \frac{\bar{\lambda}}{2}\left(\|\phi^{n+1}-\psi\|_d^2 - \|\phi^n-\psi\|_d^2 + \|\phi^{n+1}-\phi^n\|_d^2\right). \tag{3.10}$$

$$\beta\left(A_d(\phi^{n+1})-V_0,\phi^{n+1}-\phi^n\right)_d = \frac{\beta}{2}\left(\left(A_d(\phi^{n+1})-V_0\right)^2 - \left(A_d(\phi^n)-V_0\right)^2 + \left(A_d(\phi^{n+1})-A_d(\phi^n)\right)^2\right). \tag{3.11}$$

For the term $\frac{\gamma}{\varepsilon}\left(F'(\phi^n),\phi^{n+1}-\phi^n\right)_d$, we get

$$\begin{aligned} \frac{\gamma}{\varepsilon}\left(F'(\phi^n),\phi^{n+1}-\phi^n\right)_d &= \frac{\gamma}{\varepsilon}\left(F(\phi^{n+1})-F(\phi^n),\mathbf{1}\right)_d - \left(\frac{\gamma F''(\zeta^{n+1})}{2\varepsilon}(\phi^{n+1}-\phi^n),\phi^{n+1}-\phi^n\right)_d \\ &= \frac{\gamma}{\varepsilon}\left(F(\phi^{n+1})-F(\phi^n),\mathbf{1}\right)_d - \frac{\gamma F''(\bar{\zeta})}{2\varepsilon}\|\phi^{n+1}-\phi^n\|_d^2. \end{aligned} \tag{3.12}$$

Here, the function ζ^{n+1} exists because of the used Taylor expansion. Furthermore, $\bar{\zeta} \in [\phi^n, \phi^{n+1}]$ exists because of the mean value theorem of integrals. By using the definition of $\alpha(\phi)$ in Eq. (2.9), we obtain

$$\frac{1}{2}\Big(\alpha'(\phi^{n+1})|\mathbf{u}^n|^2, \phi^{n+1}-\phi^n\Big)_d = \frac{1}{2}\Big((\alpha(\phi^{n+1})-\alpha(\phi^n))\mathbf{u}^n, \mathbf{u}^n\Big)_d = \frac{1}{2}\Big(\alpha(\phi^{n+1})\mathbf{u}, \mathbf{u}\Big)_d - \Big(\alpha(\phi^n)\mathbf{u}^n, \mathbf{u}^n\Big)_d. \tag{3.13}$$

By combining the above relations, we have

$$\begin{aligned}
&-\frac{1}{\Delta t}\|\phi^{n+1}-\phi^n\|_d^2 = \frac{\gamma}{\varepsilon}\Big(F(\phi^{n+1})-F(\phi^n), \mathbf{1}\Big)_d - \frac{\gamma F''(\bar{\zeta})}{2\varepsilon}\|\phi^{n+1}-\phi^n\|_d^2 + \frac{\gamma\xi}{2\varepsilon}\|\phi^{n+1}-\phi^n\|_d^2 \\
&+ \frac{\gamma\varepsilon}{2}\Big(\|\nabla_d\phi^{n+1}\|_d^2 - \|\nabla_d\phi^n\|_d^2 + \|\nabla_d\phi^{n+1}-\nabla_d\phi^n\|_d^2\Big) + \frac{\|\mathbf{u}^n\|_d^2}{2}\Big(\alpha(\phi^{n+1})-\alpha(\phi^n), \mathbf{1}\Big)_d \\
&+ \frac{\bar{\lambda}}{2}\Big(\|\phi^{n+1}-\psi\|_d^2 - \|\phi^n-\psi\|_d^2 + \|\phi^{n+1}-\phi^n\|_d^2\Big) \\
&+ \frac{\beta}{2}\Big(\big(A_d(\phi^{n+1})-V_0\big)^2 - \big(A_d(\phi^n)-V_0\big)^2 + \big(A_d(\phi^{n+1})-A_d(\phi^n)\big)^2\Big).
\end{aligned} \tag{3.14}$$

Here, $J(\phi^{n+1}, \mathbf{u}^n) - J(\phi^n, \mathbf{u}^n)$ can be expressed as

$$\begin{aligned}
&J(\phi^{n+1}, \mathbf{u}^n) - J(\phi^n, \mathbf{u}^n) \\
&= \frac{\gamma}{\varepsilon}\Big(F(\phi^{n+1})-F(\phi^n), 1\Big)_d + \frac{\gamma\varepsilon}{2}\Big(\|\nabla_d\phi^{n+1}\|_d^2 - \|\nabla_d\phi^n\|_d^2\Big) + \frac{\|\mathbf{u}^n\|_d^2}{2}\Big(\alpha(\phi^{n+1})-\alpha(\phi^n), \mathbf{1}\Big)_d \\
&+ \frac{\bar{\lambda}}{2}\Big(\|\phi^{n+1}-\psi\|_d^2 - \|\phi^n-\psi\|_d^2\Big) + \frac{\beta}{2}\Big(\big(A_d(\phi^{n+1})-V_0\big)^2 - \big(A_d(\phi^n)-V_0\big)^2\Big).
\end{aligned} \tag{3.15}$$

By combining Eqs. (3.14) and (3.15), we get

$$\begin{aligned}
J(\phi^{n+1}, \mathbf{u}^n) - J(\phi^n, \mathbf{u}^n) = &-\frac{1}{\Delta t}\|\phi^{n+1}-\phi^n\|_d^2 + \gamma\Big(\frac{F''(\bar{\zeta})}{2\varepsilon} - \frac{\xi}{2\varepsilon}\Big)\|\phi^{n+1}-\phi^n\|_d^2 \\
&- \frac{\gamma\varepsilon}{2}\|\nabla_d\phi^{n+1}-\nabla_d\phi^n\|_d^2 - \frac{\bar{\lambda}}{2}\|\phi^{n+1}-\phi^n\|_d^2 - \frac{\beta}{2}\Big(A_d(\phi^{n+1})-A_d(\phi^n)\Big)^2 \le 0.
\end{aligned} \tag{3.16}$$

Because $F''(\phi) = 3\phi^2 - 3\phi + 1/2$ is a quadratic function and $\phi \le \mathcal{M}$, we have $F''(\mathcal{M}) \ge F''(\bar{\zeta})$. Therefore, under the condition $\xi \ge F''(\mathcal{M})$, we have $J(\phi^{n+1}, \mathbf{u}^n) - J(\phi^n, \mathbf{u}^n) \le 0$. Thus, the proof is completed. □

Lemma 3.2. *The solutions $(\phi^{n+1}, \mathbf{u}^{n+1}, \mathbf{u}^n)$ of the scheme (3.2) and (3.3) satisfy*

$$J(\phi^{n+1}, \mathbf{u}^{n+1}) \le J(\phi^{n+1}, \mathbf{u}^n)$$

Proof. By taking the inner product of Eq. (3.2) with $\mathbf{u}^{n+1} - \mathbf{u}^n$, we obtain

$$\Big(\nabla_d p^{n+1}, \mathbf{u}^{n+1}-\mathbf{u}^n\Big)_d + \Big(\mu\nabla_d\mathbf{u}^{n+1}, \nabla_d\mathbf{u}^{n+1}-\nabla_d\mathbf{u}^n\Big)_d + \Big(\alpha(\phi^{n+1})\mathbf{u}^{n+1}, \mathbf{u}^{n+1}-\mathbf{u}^n\Big)_d = \Big(\mathbf{f}, \mathbf{u}^{n+1}-\mathbf{u}^n\Big)_d. \tag{3.17}$$

Hence, we have

$$\begin{aligned}
&J(\phi^{n+1}, \mathbf{u}^{n+1}) - J(\phi^{n+1}, \mathbf{u}^n) \\
&= \frac{\mu}{2}\Big(\|\nabla_d\mathbf{u}^{n+1}\|_d^2 - \|\nabla_d\mathbf{u}^n\|_d^2\Big) + \frac{1}{2}\Big(\alpha(\phi^{n+1}), |\mathbf{u}^{n+1}|^2 - |\mathbf{u}^n|^2\Big)_d - \Big((\mathbf{u}^{n+1}, \mathbf{f})_d - (\mathbf{u}^n, \mathbf{f})_d\Big) \\
&= -\frac{\mu}{2}\|\nabla_d\mathbf{u}^{n+1}-\nabla_d\mathbf{u}^n\|_d^2 - \frac{1}{2}\Big(\alpha(\phi^{n+1}), |\mathbf{u}^{n+1}-\mathbf{u}^n|^2\Big)_d - \Big(\nabla_d p^{n+1}, \mathbf{u}^{n+1}-\mathbf{u}^n\Big)_d \\
&= -\frac{\mu}{2}\|\nabla_d\mathbf{u}^{n+1}-\nabla_d\mathbf{u}^n\|_d^2 - \frac{1}{2}\|\sqrt{\alpha(\phi^{n+1})}(\mathbf{u}^{n+1}-\mathbf{u}^n)\|_d^2 + \Big(p^{n+1}, \nabla_d\cdot\mathbf{u}^{n+1}\Big)_d - \Big(p^{n+1}, \nabla_d\cdot\mathbf{u}^n\Big)_d.
\end{aligned} \tag{3.18}$$

Because of $\nabla_d \cdot \mathbf{u} = 0$, we have $J(\phi^{n+1}, \mathbf{u}^{n+1}) - J(\phi^{n+1}, \mathbf{u}^n) \le 0$. Thus, the proof is completed. □

Theorem 3.1. *Under the condition $\xi \ge F''(\mathcal{M})$, the proposed scheme (3.1)–(3.3) is unconditionally energy stable, i.e.,*

$$J(\phi^{n+1}, \mathbf{u}^{n+1}) \le J(\phi^n, \mathbf{u}^n).$$

Proof. From Lemmas 3.1 and 3.2, we have

$$J(\phi^{n+1}, \mathbf{u}^{n+1}) \le J(\phi^{n+1}, \mathbf{u}^n) \le J(\phi^n, \mathbf{u}^n),$$

which implies our first-order scheme is indeed unconditionally energy stable. □

3.2. The second-order scheme

In order to achieve second-order accuracy in time and space, we discretize Eqs. (2.12), (2.13), and (2.19) by the following Crank–Nicolson type scheme

$$\begin{aligned}\frac{\phi^{n+1}-\phi^n}{\Delta t} &= -\frac{\gamma}{\varepsilon}\left(F'(\tilde{\phi}^{n+\frac{1}{2}})+\xi\phi^{n+\frac{1}{2}}-\xi\tilde{\phi}^{n+\frac{1}{2}}\right)+\gamma\varepsilon\Delta_d\phi^{n+\frac{1}{2}}-\overline{\lambda}(\phi^{n+\frac{1}{2}}-\psi)\\ &\quad-\frac{\alpha'(\phi^n)+\alpha'(\phi^{n+1})}{4}\frac{|\mathbf{u}^n|^2+|\mathbf{u}^{n+1}|^2}{2}-\beta\left(\frac{A_d(\phi^n)+A_d(\phi^{n+1})}{2}-V_0\right),\end{aligned} \tag{3.19}$$

$$\nabla_d p^{n+\frac{1}{2}}-\nabla_d\cdot(\mu\nabla_d\mathbf{u}^{n+\frac{1}{2}})+\frac{\alpha(\phi^n)+\alpha(\phi^{n+1})}{2}\mathbf{u}^{n+\frac{1}{2}}=\mathbf{f}, \tag{3.20}$$

$$\nabla_d\cdot\mathbf{u}^{n+1}=0, \tag{3.21}$$

where

$$\phi^{n+\frac{1}{2}}=\frac{\phi^{n+1}+\phi^n}{2},\quad \tilde{\phi}^{n+\frac{1}{2}}=\frac{3\phi^n-\phi^{n-1}}{2},\quad \mathbf{u}^{n+\frac{1}{2}}=\frac{\mathbf{u}^{n+1}+\mathbf{u}^n}{2}. \tag{3.22}$$

The outline of the main procedure of Eqs. (3.19)–(3.21) in one time step is as follows:

Step 1. Solve Eqs. (3.19)–(3.21) to get ϕ^{n+1} and $\mathbf{u}^{n+1}$ from ϕ^n and $\mathbf{u}^n$.

First, by taking the divergence operator to both sides of Eq. (3.20), we obtain

$$\Delta_d p^{n+\frac{1}{2}}+\frac{1}{4}\nabla_d\cdot((\alpha(\phi^n)+\alpha(\phi^{n+1}))(\mathbf{u}^n+\mathbf{u}^{n+1}))=\nabla_d\cdot\mathbf{f}. \tag{3.23}$$

Second, a Jacobi-type iteration method is used to solve Eqs. (3.21), (3.20), and (3.23):

$$\begin{aligned}\frac{\phi^{n+1,m+1}-\phi^n}{\Delta t} &= -\frac{\gamma}{\varepsilon}\left(F'(\tilde{\phi}^{n+\frac{1}{2}})+\frac{\xi}{2}(\phi^{n+1,m+1}+\phi^n)-\xi\tilde{\phi}^{n+\frac{1}{2}}\right)+\gamma\varepsilon\Delta_d(\phi^{n+1,m+1}+\phi^n)\\ &\quad-\overline{\lambda}\left(\frac{\phi^{n+1,m+1}+\phi^n}{2}-\psi\right)-\frac{\alpha'(\phi^n)+\alpha'(\phi^{n+1})}{4}\frac{|\mathbf{u}^n|^2+|\mathbf{u}^{n+1,m}|^2}{2}-\beta\left(\frac{A_d(\phi^n)+A_d(\phi^{n+1,m+1})}{2}-V_0\right),\end{aligned} \tag{3.24}$$

$$A_d(\phi^{n+1,m+1})=(\phi^{n+1,m+1},\mathbf{1})_d, \tag{3.25}$$

$$\Delta_d p^{n+\frac{1}{2}}+\frac{1}{4}\nabla(\alpha(\phi^n)+\alpha(\phi^{n+1,m+1}))\cdot(\mathbf{u}^n+\mathbf{u}^{n+1,m})=\nabla_d\cdot\mathbf{f}, \tag{3.26}$$

$$\nabla_d p^{n+\frac{1}{2}}-\frac{1}{2}\nabla_d\cdot(\mu\nabla_d(\mathbf{u}^n+\mathbf{u}^{n+1,m+1}))+\frac{1}{4}(\alpha(\phi^n)+\alpha(\phi^{n+1,m+1}))(\mathbf{u}^n+\mathbf{u}^{n+1,m+1})=\mathbf{f}. \tag{3.27}$$

Beginning with $\phi^{n+1,0}=2\phi^n-\phi^{n-1}$ and $\mathbf{u}^{n+1,0}=2\mathbf{u}^n-\mathbf{u}^{n-1}$, we solve Eqs. (3.24)–(3.27) by using the preconditioning conjugate gradient method. The computation is performed until the error is smaller than a given tolerance as

$$\|\phi^{n+1,m+1}-\phi^{n+1,m}\|_d^2+\|\mathbf{u}^{n+1,m+1}-\mathbf{u}^{n+1,m}\|_d^2<tol.$$

Then, we will set $\phi^{n+1}=\phi^{n+1,m+1}$ and $\mathbf{u}^{n+1}=\mathbf{u}^{n+1,m+1}$. The residual error converges rather quickly to a tolerance $tol=1e{-}5$ in 3–5 iterations. Following Step 1–Step 2, one iteration of computational simulation is completed. The existence of a unique solution to Eqs. (3.24)–(3.27) can be guaranteed because Eq. (3.24) is a linear system of $\phi^{n+1,m+1}$ and Eqs. (3.26)–(3.27) is a linear system of $\mathbf{u}^{n+1,m+1}$ and $p^{n+\frac{1}{2}}$. This shows existence and uniqueness of $(\phi^{n+1},\mathbf{u}^{n+1},p^{n+\frac{1}{2}})$ to Eqs. (3.19)–(3.21). Before we prove the stability of our method, we define the discrete pseudo energy as

$$\tilde{J}\left(\phi^{n+1},\phi^n,\mathbf{u}^{n+1}\right)=J(\phi^{n+1},\mathbf{u}^{n+1})+\frac{\xi-F''(\sigma^{n,n+1})}{4}\|\phi^{n+1}-\phi^n\|_d^2. \tag{3.28}$$

Here, $\sigma^{n,n+1}$ satisfies the following equation

$$\begin{aligned}\left(F'\left(\tilde{\phi}^{n+\frac{1}{2}}\right),\phi^{n+1}-\phi^n\right)_d &= \left(F\left(\phi^{n+1}\right)-F\left(\phi^n\right),\mathbf{1}\right)_d\\ &\quad-\frac{F''(\sigma^{n,n+1})}{4}\left(\|\phi^{n+1}-\phi^n\|_d^2-\|\phi^n-\phi^{n-1}\|_d^2+\|\phi^{n+1}-2\phi^n+\phi^{n-1}\|_d^2\right).\end{aligned} \tag{3.29}$$

Theorem 3.2. *Under the condition that $\xi\geq F''(\mathcal{M})$, the solutions $(\phi^{n+1},\phi^n,\mathbf{u}^{n+1},\mathbf{u}^n)$ of the scheme (3.19)–(3.21) satisfy*

$$\tilde{J}\left(\phi^{n+1},\phi^n,\mathbf{u}^{n+1}\right)\leq\tilde{J}\left(\phi^n,\phi^{n-1},\mathbf{u}^n\right).$$

Proof. By taking the inner product of Eq. (3.20) with $\mathbf{u}^{n+1}-\mathbf{u}^n$, we obtain

$$\begin{aligned}&\frac{1}{2}\left(\nabla_d p^n+\nabla_d p^{n+1},\mathbf{u}^{n+1}-\mathbf{u}^n\right)_d+\frac{\mu}{2}\left(\nabla_d\mathbf{u}^n+\nabla_d\mathbf{u}^{n+1},\nabla_d\mathbf{u}^{n+1}-\nabla_d\mathbf{u}^n\right)_d\\ &+\frac{1}{4}\left(\alpha(\phi^n)+\alpha(\phi^{n+1}),|\mathbf{u}^{n+1}|^2-|\mathbf{u}^n|^2\right)_d-\left(\mathbf{f},\mathbf{u}^{n+1}-\mathbf{u}^n\right)_d=0,\end{aligned} \tag{3.30}$$

$$\begin{aligned}
&\frac{\mu}{2}\left(\|\nabla_d \mathbf{u}^{n+1}\|_d^2 - \|\nabla_d \mathbf{u}^n\|_d^2\right) + \frac{1}{2}\left(\alpha(\phi^{n+1}), |\mathbf{u}^{n+1}|^2\right)_d - \frac{1}{2}\left(\alpha(\phi^n), |\mathbf{u}^n|^2\right)_d - \left(\mathbf{u}^{n+1}, \mathbf{f}\right)_d - \left(\mathbf{u}^n, \mathbf{f}\right)_d \\
&= \frac{1}{2}\left(p^n + p^{n+1}, \nabla_d \cdot \mathbf{u}^{n+1} - \nabla_d \cdot \mathbf{u}^n\right)_d + \frac{1}{4}\left(\alpha(\phi^{n+1}) - \alpha(\phi^n), |\mathbf{u}^{n+1}|^2 + |\mathbf{u}^n|^2\right)_d \\
&= \left(\alpha(\phi^{n+1}) - \alpha(\phi^n), \frac{|\mathbf{u}^n|^2 + |\mathbf{u}^{n+1}|^2}{4}\right)_d.
\end{aligned} \tag{3.31}$$

Taking inner product of Eq. (3.19) with $-(\phi^{n+1} - \phi^n)$, we obtain

$$\begin{aligned}
&-\frac{1}{\Delta t}\|\phi^{n+1} - \phi^n\|_d^2 = \frac{\gamma}{\varepsilon}\left(F'(\tilde{\phi}^{n+\frac{1}{2}}), \phi^{n+1} - \phi^n\right)_d + \frac{\xi\gamma}{\varepsilon}\left(\phi^{n+\frac{1}{2}} - \tilde{\phi}^{n+\frac{1}{2}}, \phi^{n+1} - \phi^n\right)_d \\
&- \varepsilon\gamma\left(\Delta_d \phi^{n+\frac{1}{2}}, \phi^{n+1} - \phi^n\right)_d + \left(\frac{\alpha'(\phi^n) + \alpha'(\phi^{n+1})}{4}\frac{|\mathbf{u}^n|^2 + |\mathbf{u}^{n+1}|^2}{2}, \phi^{n+1} - \phi^n\right)_d \\
&+ \bar{\lambda}\left(\phi^{n+\frac{1}{2}} - \psi, \phi^{n+1} - \phi^n\right)_d + \frac{\beta}{2}\left(A_d(\phi^{n+1}) + A_d(\phi^n) - 2V_0, \phi^{n+1} - \phi^n\right)_d.
\end{aligned} \tag{3.32}$$

Each term of Eq. (3.32) can be expressed as follows:

$$-\varepsilon\gamma\left(\Delta_d \phi^{n+\frac{1}{2}}, \phi^{n+1} - \phi^n\right)_d = \frac{\gamma\varepsilon}{2}\|\nabla_d \phi^{n+1}\|_d^2 - \frac{\gamma\varepsilon}{2}\|\nabla_d \phi^n\|_d^2, \tag{3.33}$$

$$\bar{\lambda}\left(\phi^{n+\frac{1}{2}} - \psi, \phi^{n+1} - \phi^n\right)_d = \frac{\bar{\lambda}}{2}\|\phi^{n+1} - \psi\|_d^2 - \frac{\bar{\lambda}}{2}\|\phi^n - \psi\|_d^2, \tag{3.34}$$

$$\begin{aligned}
&\beta\left(\frac{A_d(\phi^{n+1}) + A_d(\phi^n)}{2} - V_0, \phi^{n+1} - \phi^n\right)_d = \frac{\beta}{2}(A_d(\phi^{n+1}) + A_d(\phi^n) - 2V_0)\left(\phi^{n+1} - \phi^n, \mathbf{1}\right)_d \\
&= \frac{\beta}{2}\left(A_d(\phi^{n+1}) - V_0 + A_d(\phi^n) - V_0\right)\left(A_d(\phi^{n+1}) - V_0 - (A_d(\phi^n) - V_0)\right) \\
&= \frac{\beta}{2}\left(A_d\left(\phi^{n+1}\right) - V_0\right)^2 - \frac{\beta}{2}\left(A_d\left(\phi^n\right) - V_0\right)^2,
\end{aligned}$$

$$\frac{\xi\gamma}{\varepsilon}\left(\phi^{n+\frac{1}{2}} - \tilde{\phi}^{n+\frac{1}{2}}, \phi^{n+1} - \phi^n\right)_d = \frac{\xi\gamma}{4\varepsilon}\left(\|\phi^{n+1} - \phi^n\|_d^2 - \|\phi^n - \phi^{n-1}\|_d^2 + \|\phi^{n+1} - 2\phi^n + \phi^{n-1}\|_d^2\right). \tag{3.35}$$

Here, we can pull $A_d(\phi^{n+1})$ and $A_d(\phi^n)$ out of the discretized scalar product, because these two terms only depend on the temporal discretization. Taylor expansion formula and mean value theorem of integrals are applied to obtain the expression of the first right term in Eq. (3.32):

$$\begin{aligned}
&\left(F\left(\phi^{n+1}\right), \mathbf{1}\right)_d - \left(F\left(\tilde{\phi}^{n+\frac{1}{2}}\right), \mathbf{1}\right)_d \\
&= \left(F'\left(\tilde{\phi}^{n+\frac{1}{2}}\right), \phi^{n+1} - \tilde{\phi}^{n+\frac{1}{2}}\right)_d + \left(\frac{F''(\zeta_1^{n+1})}{2}(\phi^{n+1} - \tilde{\phi}^{n+\frac{1}{2}}), \phi^{n+1} - \tilde{\phi}^{n+\frac{1}{2}}\right)_d \\
&= \left(F'\left(\tilde{\phi}^{n+\frac{1}{2}}\right), \phi^{n+1} - \tilde{\phi}^{n+\frac{1}{2}}\right)_d + \frac{F''\left(\hat{\zeta}_1^{n+1}\right)}{2}\left\|\phi^{n+1} - \tilde{\phi}^{n+\frac{1}{2}}\right\|_d^2
\end{aligned} \tag{3.36}$$

and

$$\begin{aligned}
&\left(F\left(\phi^n\right), \mathbf{1}\right)_d - \left(F\left(\tilde{\phi}^{n+\frac{1}{2}}\right), \mathbf{1}\right)_d \\
&= \left(F'\left(\tilde{\phi}^{n+\frac{1}{2}}\right), \phi^n - \tilde{\phi}^{n+\frac{1}{2}}\right)_d + \left(\frac{F''(\zeta_2^n)}{2}(\phi^n - \tilde{\phi}^{n+\frac{1}{2}}), \phi^n - \tilde{\phi}^{n+\frac{1}{2}}\right)_d \\
&= \left(F'\left(\tilde{\phi}^{n+\frac{1}{2}}\right), \phi^n - \tilde{\phi}^{n+\frac{1}{2}}\right)_d + \frac{F''\left(\hat{\zeta}_2^n\right)}{2}\left\|\phi^n - \tilde{\phi}^{n+\frac{1}{2}}\right\|_d^2.
\end{aligned} \tag{3.37}$$

Here, two functions ζ_1^{n+1}, ζ_2^n and two constants $\hat{\zeta}_2^{n+1}$, $\hat{\zeta}_2^n$ exist because of mean value theorem of integrals. Furthermore, there exists $\sigma^{n+1,n} \in [\hat{\zeta}_2^n, \hat{\zeta}_1^{n+1}]$ which satisfies the following equation

$$\begin{aligned}
&\left(F'\left(\tilde{\phi}^{n+\frac{1}{2}}\right), \phi^{n+1} - \phi^n\right)_d \\
&= \left(F\left(\phi^{n+1}\right) - F\left(\phi^n\right), \mathbf{1}\right)_d + \frac{F''(\sigma^{n+1,n})}{4}(\|\phi^n - \phi^{n-1}\|_d^2 - \|\phi^{n+1} - \phi^n\|_d^2 - \|\phi^{n+1} - 2\phi^n + \phi^{n-1}\|_d^2).
\end{aligned} \tag{3.38}$$

Because $\alpha(\phi) = \alpha_\varepsilon \phi$, we have the following equation

$$\begin{aligned}&\left(\frac{\alpha'(\phi^n)+\alpha'(\phi^{n+1})}{4}\frac{|\mathbf{u}^n|^2+|\mathbf{u}^{n+1}|^2}{2}, \phi^{n+1}-\phi^n\right)_d \\ &= \left(\frac{\alpha'(\phi^n)+\alpha'(\phi^{n+1})}{2}\left(\phi^{n+1}-\phi^n\right), \frac{|\mathbf{u}^n|^2+|\mathbf{u}^{n+1}|^2}{4}\right)_d = \left(\alpha(\phi^{n+1})-\alpha(\phi^n), \frac{|\mathbf{u}^n|^2+|\mathbf{u}^{n+1}|^2}{4}\right)_d.\end{aligned} \tag{3.39}$$

Combining Eqs. (3.33)–(3.39), we have

$$\begin{aligned}&\frac{\gamma}{\varepsilon}\left(F\left(\phi^{n+1}\right)-F\left(\phi^n\right), \mathbf{1}\right)_d + \frac{\xi\gamma}{4\varepsilon}\left(\|\phi^{n+1}-\phi^n\|_d^2 - \|\phi^n-\phi^{n-1}\|_d^2 + \|\phi^{n+1}-2\phi^n+\phi^{n-1}\|_d^2\right) \\ &+ \frac{\gamma F''(\sigma^{n+1,n})}{4\varepsilon}\left(-\|\phi^{n+1}-\phi^n\|_d^2 + \|\phi^n-\phi^{n-1}\|_d^2 - \|\phi^{n+1}-2\phi^n+\phi^{n-1}\|_d^2\right) - \frac{\beta}{2}\left(A_d\left(\phi^n\right)-V_0\right)^2 \\ &+ \frac{\gamma\varepsilon}{2}\|\nabla_d\phi^{n+1}\|_d^2 - \frac{\gamma\varepsilon}{2}\|\nabla_d\phi^n\|_d^2 + \frac{\overline{\lambda}}{2}\|\phi^{n+1}-\psi\|_d^2 - \frac{\overline{\lambda}}{2}\|\phi^n-\psi\|_d^2 + \frac{\beta}{2}\left(A_d\left(\phi^{n+1}\right)-V_0\right)^2 \\ &= -\left(\alpha(\phi^{n+1})-\alpha(\phi^n), \frac{|\mathbf{u}^n|^2+|\mathbf{u}^{n+1}|^2}{4}\right)_d - \frac{1}{\Delta t}\|\phi^{n+1}-\phi^n\|_d^2.\end{aligned} \tag{3.40}$$

Then, by combining Eqs. (3.31) and (3.40), we can obtain

$$\tilde{J}\left(\phi^{n+1}, \phi^n, \mathbf{u}^{n+1}\right) - \tilde{J}\left(\phi^n, \phi^{n-1}, \mathbf{u}^n\right) = -\frac{1}{\Delta t}\|\phi^{n+1}-\phi^n\|_d^2 - \frac{\xi - F''(\sigma^{n+1,n})}{4\varepsilon}\gamma\left\|\phi^{n+1}-2\phi^n+\phi^{n-1}\right\|_d^2 \le 0.$$

Here, the condition $\xi \ge F''(\mathcal{M})$ is used. The proof is completed. □

Lemma 3.3. *If $\xi \ge F''(\mathcal{M})$, then $J\left(\phi^{n+1}, \mathbf{u}^{n+1}\right) \le \tilde{J}\left(\phi^{n+1}, \phi^n, \mathbf{u}^{n+1}\right)$.*

Proof. By Eq. (3.28), we can have

$$J\left(\phi^{n+1}, \mathbf{u}^{n+1}\right) - \tilde{J}\left(\phi^{n+1}, \phi^n, \mathbf{u}^{n+1}\right) = -\frac{\xi - F''(\sigma^{n+1,n})}{4}\|\phi^{n+1}-\phi^n\|_d^2 \le 0. \quad \square \tag{3.41}$$

Theorem 3.3. *Suppose that $\{\phi^n, \mathbf{u}^n\}_{n=1}^N$ are a sequence of solution pairs of the scheme (3.19)–(3.21) with the starting values $\{\phi^0, \mathbf{u}^0\}$ and $\{\phi^{-1}, \mathbf{u}^{-1}\}$, where $\phi^0 = \phi^{-1}$ and $\mathbf{u}^0 = \mathbf{u}^{-1}$. Then, we have*

$$J(\phi^{n+1}, \mathbf{u}^{n+1}) \le \tilde{J}\left(\phi^{n+1}, \phi^n, \mathbf{u}^{n+1}\right) \le J(\phi^0, \mathbf{u}^0).$$

Proof. By Theorem 3.2, Lemma 3.3 and $\phi^0 = \phi^{-1}$, a chain of inequalities can be obtained

$$J(\phi^{n+1}, \mathbf{u}^{n+1}) \le \tilde{J}\left(\phi^{n+1}, \phi^n, \mathbf{u}^{n+1}\right) \le \tilde{J}\left(\phi^n, \phi^{n-1}, \mathbf{u}^n\right) \ldots \le \tilde{J}\left(\phi^0, \phi^{-1}, \mathbf{u}^0\right) = J(\phi^0, \mathbf{u}^0). \tag{3.42}$$

Therefore, the discrete version of the original energy is bounded and the discrete pseudo total energy is non-increasing. Therefore, our proposed method (3.19)–(3.21) is unconditionally pseudo energy stable. □

Remark 2. It should be noted that the total energy dissipation has been proved in Theorems 3.1 and 3.3. By using the first-order numerical scheme in Section 3.1, the convergence of original optimization problem can be directly proved because we use a gradient descent flow to obtain the governing equation and have proved that $J(\phi^{n+1}, \mathbf{u}^{n+1}) \le J(\phi^n, \mathbf{u}^n)$. However, for the second-order scheme, the pseudo energy is proved to be non-increased and the loss function of the original optimization problem is bounded, i.e. $J(\phi^{n+1}, \mathbf{u}^{n+1}) \le \tilde{J}\left(\phi^{n+1}, \phi^n, \mathbf{u}^{n+1}\right)$. Despite it being difficult to exactly prove that the original optimization problem (Eqs. (2.11)–(2.15)) follows a energy dissipation law or not, the results of the numerical tests presented in Section 4 indicate that the original energy $J(\phi, \mathbf{u})$ is non-increasing.

4. Numerical results

In this section, extensive numerical tests are performed to validate the accuracy and efficiency of the proposed schemes. The domain boundary consists of $\partial\Omega = \partial\Omega_{wall} \bigcup \partial\Omega_{in} \bigcup \partial\Omega_{out}$, where $\partial\Omega_{wall}$, $\partial\Omega_{in}$, and $\partial\Omega_{out}$ are the wall, inlet, and outlet boundaries, respectively. Here, the velocities on the boundary are defined as

$$\mathbf{u}|_{\partial\Omega} = \begin{cases} \mathbf{u}|_{\partial\Omega_{wall}} \text{ is zero,} \\ \mathbf{u}|_{\partial\Omega_{in}} \text{ is Dirichlet boundary with a parabolic profile,} \\ \mathbf{u}|_{\partial\Omega_{out}} \text{ is Dirichlet boundary with a parabolic profile.} \end{cases}$$

We choose the Dirichlet boundary conditions with a parabolic profile and its mean inflow velocity $\bar{g}$ in a rectangular domain $\Omega = [0, 1] \times [0, 1]$. The boundary conditions have the same form on both inflow and outflow boundaries and lead

Table 1
Errors and convergence results with various mesh grids for the first-order scheme. Here $\Delta t = 0.001h^2$ is fixed.

h	$1/32 - 1/64$		$1/64 - 1/128$		$1/128 - 1/256$
L^2-error of u	8.331E−4		2.080E−4		5.201E−5
Rate		2.00		2.01	
L^2-error of v	7.968E−4		1.991E−4		4.665E−5
Rate		1.97		1.99	
L^2-error of p	5.864E−4		1.466E−4		3.665E−5
Rate		1.98		2.02	
L^2-error of ϕ	1.233E−4		3.056E−5		7.665E−6
Rate		2.01		2.00	

Table 2
Errors and convergence results with various mesh grids for the second-order scheme. Here $\Delta t = 0.001h$ is fixed.

h	$1/32 - 1/64$		$1/64 - 1/128$		$1/128 - 1/256$
L^2-error of u	8.273E−4		2.058E−4		4.975E−5
Rate		1.99		1.90	
L^2-error of v	7.950E−4		1.988E−4		4.961E−5
Rate		1.96		2.02	
L^2-error of p	5.651E−4		1.412E−4		3.531E−5
Rate		1.95		1.97	
L^2-error of ϕ	1.199E−4		2.991E−5		7.627E−6
Rate		2.00		1.97	

to a divergence free solution. Unless otherwise specified, we use the following parameter values: $h = 1/256$, $\Delta t = 0.1h$, $\varepsilon = \sqrt{2}h/\tanh^{-1}(0.9)$, $\alpha_\epsilon = 200$, $\mathbf{f} = \mathbf{0}$, i.e., no fluid body forces. In our proof, the stabilizing parameter ξ is chosen to be $\xi \geq F''(\mathcal{M}) = 3\mathcal{M}^2 - 3\mathcal{M} + 1/2$ to make the pseudo energy strictly non-increasing. However, in practical simulation, ξ may be chosen as $\xi = 1/2$ for the initial condition $\phi^0 \in [0, 1]$ because the absolute value of $\tilde{\zeta}$ may be much smaller than $\mathcal{M}$. Unless otherwise specified, we will use $\xi = 1/2$ throughout this paper. Note that we use a conjugate gradient method preconditioned by the multigrid method to solve the system (3.1)–(3.3) and (3.24)–(3.27).

4.1. Convergence test

In this test, we verify the time and space convergence rates of the proposed first-order and second-order accurate schemes. We choose the initial conditions as $\phi(x, y, 0) = 0.4 + 0.1\,(\sin(2\pi x) + \cos(2\pi y))$, $u(x, y, 0) = 0.5(x - 0.5)^2$, $v(x, y, 0) = 0.5(y - 0.5)^2$, and $p = 0.5(\sin(2\pi x) + \cos(2\pi y))$. To obtain the convergence rate for spatial discretization, we perform a number of simulations with increasing finer grids $32 \times 32, 64 \times 64, 128 \times 128, 256 \times 256$ on the computational domain $\Omega = (0, 1) \times (0, 1)$. We run the simulations up to the time $T = 4\text{E}{-6}$ with $\Delta t = 0.001h^2$ and $\Delta t = 0.001h$ for the first- and second-order schemes, respectively. The other parameters are chosen as $\beta = 200$ and the tolerance error as 1E−15. Because there is no exact solution, we define the Cauchy error of a grid as the difference between that grid and the average of the fine solution neighboring it as following: $e_{i,j}^{\phi(h/\frac{h}{2})} = \phi_{i,j}^h - \frac{\phi_{2i-1,2j-1}^{h/2} + \phi_{2i-1,2j}^{h/2} + \phi_{2i,2j-1}^{h/2} + \phi_{2i,2j}^{h/2}}{4}$. The rate of convergence can be defined as the ratio of successive error: $\log_2(\|e^h\|_2/\|e^{\frac{h}{2}}\|_2)$, where $\|e\|_2$ is the L_2-norm defined as $\|e\|_2 = \sqrt{\Sigma_{i=1}^{N_x}\Sigma_{j=1}^{N_y} e_{i,j}^2/(N_x N_y)}$. The error between the numerical solution and the reference solution satisfies $\|e\|_2 = O(\Delta t^m + h^n)$ in analysis. If we set $\Delta t = ch^{n/m}$, then $\|e\|_2$ will approach to $O(h^n)$. Here, c is a constant. Then, the rate $\log_2(\|e_h\|_2/\|e_{\frac{h}{2}}\|_2)$ will become n. The errors and convergence rates are presented in Tables 1–2. The results suggest that our schemes Eqs. (3.1)–(3.3) and (3.19)–(3.21) are both indeed second-order accurate in space. Observing these results, we can see that the convergence results are similar, when we use the time step $0.001h^2$ and $0.001h$ for the first-order and the second-order schemes, respectively. However, the used time step in second-order scheme is much larger than the one used in the first-order scheme.

To obtain the convergence rate for temporal discretization, we fix $h = 1/128$ and choose several time steps $\Delta t = 0.001h$, $0.002h$, $0.004h$, and $0.008h$. We run the simulations up to the time $T = 4\text{E}{-6}$ for the first- and second-order schemes. The l_2-norm error of a grid to be $e_{i,j}^{\phi(t/\frac{t}{2})} = \phi_{i,j}^t - \phi_{i,j}^{\frac{t}{2}}$. The errors and convergence rates are presented in Tables 3–4. The results suggest that our schemes Eqs. (3.1)–(3.3) and (3.19)–(3.21) are first-order and second-order accurate in time, respectively.

4.2. Topology optimization of diffuser in 2D

In this test, we impose the inflow/outflow velocity at the left/right boundary of a diffuser as shown in Fig. 1. We set $\bar{g} = 1$ and $\bar{g} = 3$ for the inflow and outflow velocities, respectively. The other parameters used are $\beta = 2000$, $V_0 = 0.55$,

Table 3
Errors and convergence results with various time steps for the first-order scheme. Here $h = 1/128$ is fixed.

Δt	$0.008h - 0.004h$		$0.004h - 0.002h$		$0.002h - 0.001h$
L^2-error of u	5.693E−5		2.847E−5		1.422E−5
Rate		1.00		0.98	
L^2-error of v	5.836E−5		2.918E−5		1.456E−5
Rate		0.95		0.97	
L^2-error of p	2.656E−5		1.327E−5		6.636E−6
Rate		1.01		0.99	
L^2-error of ϕ	7.912E−6		3.742E−6		1.835E−6
Rate		1.08		1.02	

Table 4
Errors and convergence results with various time steps for the second-order scheme. Here $h = 1/128$ is fixed.

Δt	$0.008h - 0.004h$		$0.004h - 0.002h$		$0.002h - 0.001h$
L^2-error of u	5.681E−5		2.839E−5		1.411E−5
Rate		1.01		1.02	
L^2-error of v	5.623E−5		2.811E−5		1.404E−5
Rate		0.99		1.01	
L^2-error of p	2.546E−5		1.271E−5		6.365E−6
Rate		0.98		0.96	
L^2-error of ϕ	7.899E−6		3.729E−6		1.716E−6
Rate		1.06		1.02	

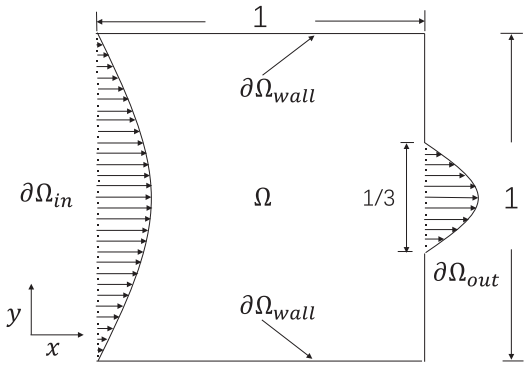

Fig. 1. Schematic illustration of inflow and outflow.

and $\gamma = 10$. The initial distribution of fluid is restricted in the middle of the design domain. Fig. 2 shows the time evolution of topology optimization with the first-order (top row) and second-order (bottom row) schemes. The computational times are drawn below each figure. Here, $\Delta t = 0.1h$ is used. We can find that the interface of the fluid region gradually becomes smooth. The inlet diameter becomes wider while the outlet diameter becomes narrower. Furthermore, the second-order scheme (3.19)–(3.21) generates the accurate solutions quicker than the first-order scheme (3.1)–(3.3) does as shown in Fig. 2 because the result obtained by using the first-order scheme at time $t = 3$ is similar with that obtained by using the second-order scheme at time $t = 1$.

To investigate the dependence of the computational process on ξ, we use two different $\xi = 1/4$ and $\xi = 1$. The other parameters and initial conditions are used as same as those in the above test. Fig. 3 shows the optimal designs obtained at time $t = 3$. (a) and (b) are the results with first-order scheme. (c) and (d) are the results with second-order scheme. From these results, we can observe that the optimal designs obtained by using $\xi = 1/4$ are in good agreement with these results obtained by using $\xi = 1$. Therefore unless otherwise specified, we will use $\xi = 1/2$ and only adopt the second-order scheme to perform next several experiments.

4.3. Stability of our proposed schemes

Energy stability has been widely investigated for numerical schemes of classic PDE-based phase field models. To demonstrate the stability of our proposed schemes (3.1)–(3.3) and (3.19)–(3.21), we perform two numerical experiments with large time steps $\Delta t = 100$. The calculations are run up to final time $T = 15\,000$. The results are shown in Fig. 4. We can see that the total energies of our first- and second-order schemes are non-increasing, which implies that our schemes are unconditionally energy stable.

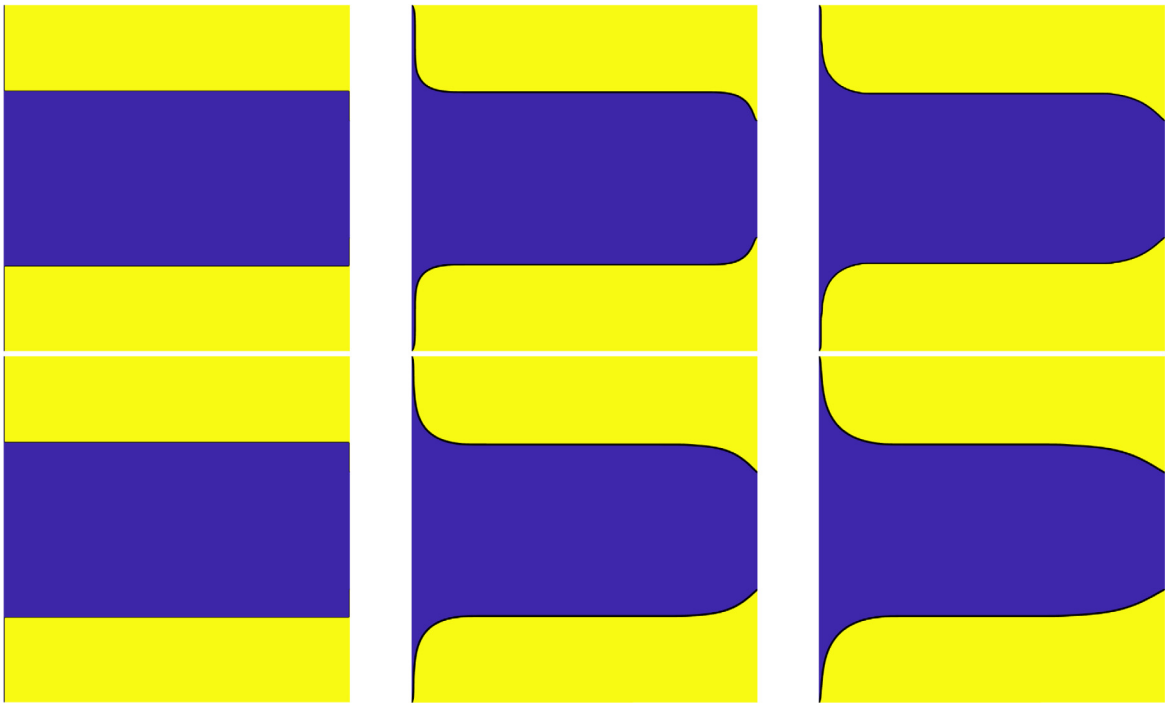

Fig. 2. The time evolution of topology optimization with the first-order (top row) and second-order (bottom row) schemes. The computational times are drawn below each figure. Here, $\Delta t = 0.1h$ is used.

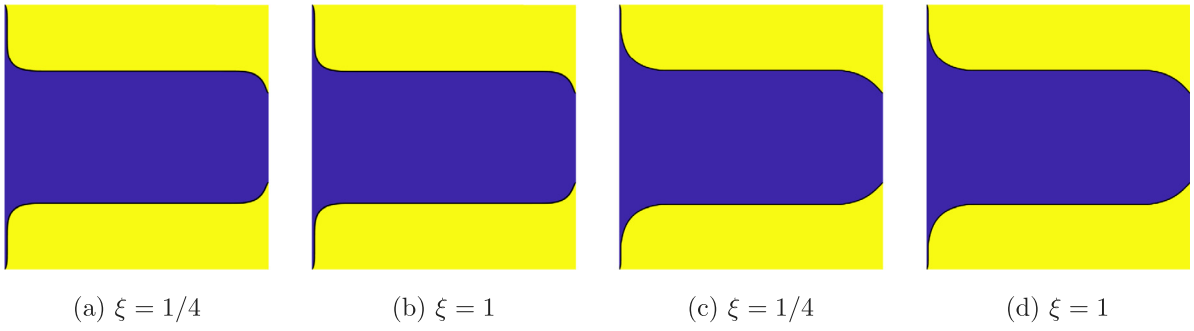

Fig. 3. The optimal designs obtained with different ξ at time $t = 3$. (a) and (b) are the results with first-order scheme. (c) and (d) are the results with second-order scheme.

4.4. Comparison with the decoupled numerical scheme

The decoupled scheme is a simple and efficient method for the fluid topology optimization. Our first-order scheme is a decoupled scheme, however, the second-order scheme is a coupled one. We can design a decoupled Crank–Nicolson scheme with second-order accuracy in time and space. Here, only three elliptic equations with constant coefficients should be solved at each time step, which makes it easy to implement. However, the total energy of the decoupled scheme may be increased. For example, we can replace the term $\mathbf{u}^{n+\frac{1}{2}}$ in Eq. (3.19) by $\tilde{\mathbf{u}}^{n+\frac{1}{2}}$ as following:

$$\begin{aligned}\frac{\phi^{n+1}-\phi^{n}}{\Delta t} = &-\frac{\gamma}{\varepsilon}\Big(F^{'}(\tilde{\phi}^{n+\frac{1}{2}})+\xi\phi^{n+\frac{1}{2}}-\xi\tilde{\phi}^{n+\frac{1}{2}}\Big)+\gamma\varepsilon\Delta_d\phi^{n+\frac{1}{2}}-\overline{\lambda}(\phi^{n+\frac{1}{2}}-\psi)\\ &-\frac{\alpha^{'}(\phi^{n})+\alpha^{'}(\phi^{n+1})}{4}\frac{|\mathbf{u}^{n}|^{2}+|\tilde{\mathbf{u}}^{n+1}|^{2}}{2}-\beta\Big(\frac{A_d(\phi^{n})+A_d(\phi^{n+1})}{2}-V_0\Big),\end{aligned} \tag{4.1}$$

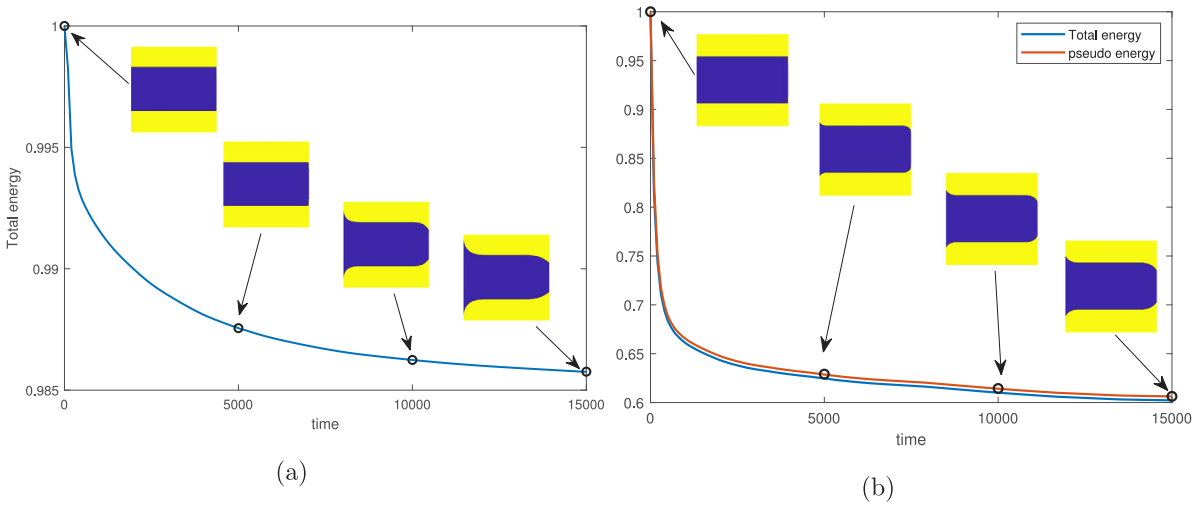

Fig. 4. The time evolution of the total energy of the first-order (a) and second-order (b) schemes under a large time step $\Delta t = 100$. Snapshots of the phase fields are shown.

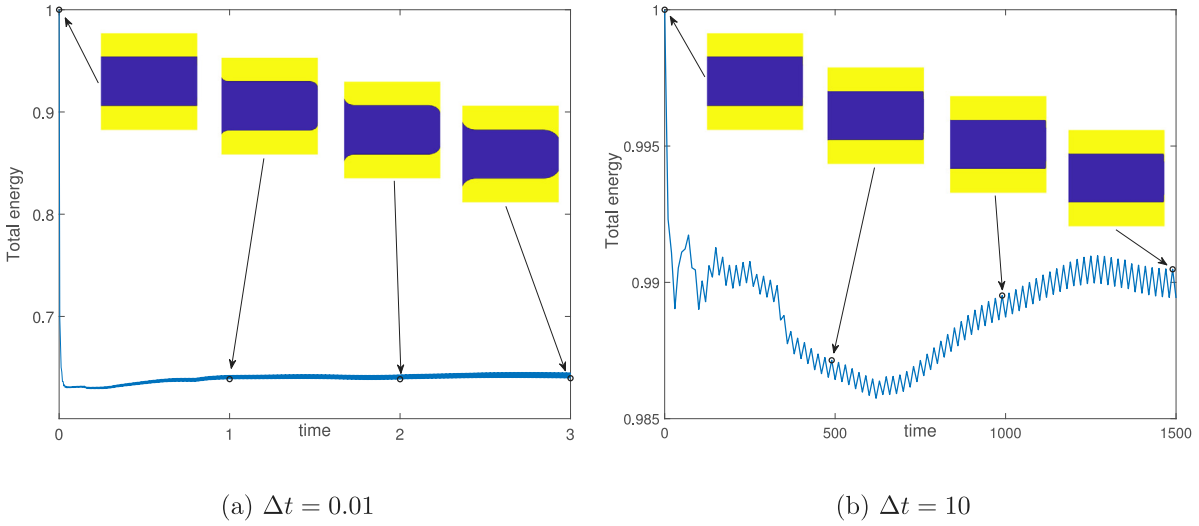

Fig. 5. The time evolution of the decoupled scheme with different time steps.

$$\nabla_d p^{n+\frac{1}{2}} - \nabla_d \cdot (\mu \nabla_d \mathbf{u}^{n+\frac{1}{2}}) + \frac{\alpha(\phi^n) + \alpha(\phi^{n+1})}{2} \mathbf{u}^{n+\frac{1}{2}} = \mathbf{f}, \tag{4.2}$$

$$\nabla_d \cdot \mathbf{u}^{n+1} = 0. \tag{4.3}$$

Eqs. (4.1)–(4.3) are a decoupled numerical scheme because we can firstly calculate ϕ^{n+1} by Eq. (4.1) and then use Eqs. (4.2)–(4.3) to calculate $\mathbf{u}^{n+1}$ and p^{n+1}. In order to compare with the decoupled numerical scheme, we use the same parameters and initial conditions in Section 4.3. The experimental results are shown in Fig. 5. The time steps $\Delta t = 0.01$ and $\Delta t = 10$ are used in Fig. 5(a) and (b), respectively. Observing these results, we can find that even though the solutions do not blowup, the total energies are increased. Furthermore, if the time step is much higher, the solution of ϕ will become same as the initial condition.

4.5. Effect of the parameter γ

Because $E(\phi) = \int_\Omega \left(\frac{\varepsilon}{2} |\nabla \phi|^2 + \frac{1}{\varepsilon} F(\phi) \right) d\mathbf{x}$ is proportional to the length of the optimal shape of Ω_0. In general, if γ is large, then the perimeter functional $\Gamma(\Omega_0)$ is dominant and the interface of the shape is smooth. In this section, we will consider the effect of γ. Here $\xi = 1/2$ is fixed. Under the same conditions in Section 4.2, we set $\gamma = 10$, 100, and 1000.

(a) $\gamma = 10$ (b) $\gamma = 100$ (c) $\gamma = 10000$

Fig. 6. The effect of γ on the optimal results. The values of γ are shown below each figure.

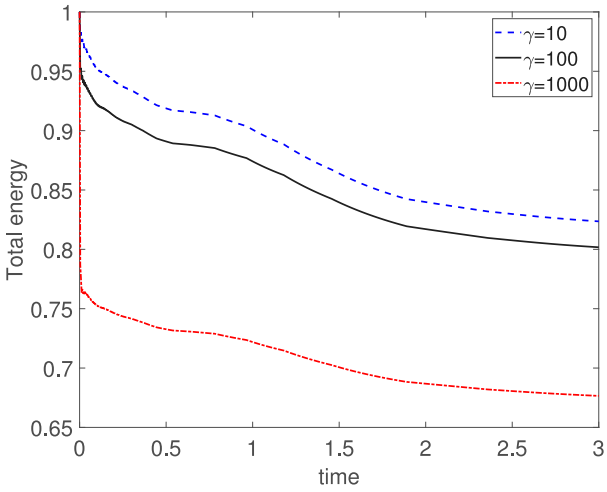

Fig. 7. The evolutions of total energy with $\gamma = 10$,100 and 1000. Note that we have normalized the total energy by using the total energy at the initial time.

The optimal designs obtained are shown in Fig. 6, from which we can see that the optimal results seem similar but the volumes of fluid region are apparently different. Fig. 7 describes the evolution of energy corresponding to different values of γ. Note that we have normalized the total energy by using the total energy at the initial time. For all the cases, the total energy functionals are decreasing.

4.6. Effect of the external force **f**

Next, we study the effect of the external force **f**, which is imposed in the local circular region with center $[0.5,\ 0.5]$ and radius $r = 0.1$. The inflow and outflow boundary conditions are chosen as the same as those in Section 4.2. The initial distribution of fluid is restricted in the design domain $(0.25,\ 0.75) \times (0,\ 1)$. Fig. 8 shows the optimal designs obtained with different external force terms. From left to right, the external force terms are $[-150, 0]$, $[0,\ 0]$, and $[150,\ 0]$, respectively. Observing these results, we can find that the direction and the magnitude of the force affected greatly on the optimal design. Due to the existence of the external force, the incompressibility condition prevents the fluid from having a much larger or smaller velocity at the middle of the pipe than at the inlet and outlet. Therefore, the optimal designs will become shaped at the middle of the pipe.

4.7. Effect of initial configurations

To test the effect of initial configurations, we perform a double pipes example as shown in Fig. 9. The inflow and outflow are located in several discontinuous sections of Dirichlet boundaries. The centers of different sections are $[0, 1/4]$, $[0, 3/4]$, $[1, 1/4]$ and $[1, 3/4]$. Here, we set $\beta = 2000$ and $\bar{g} = 1/3$ for the inflow and outflow velocities,

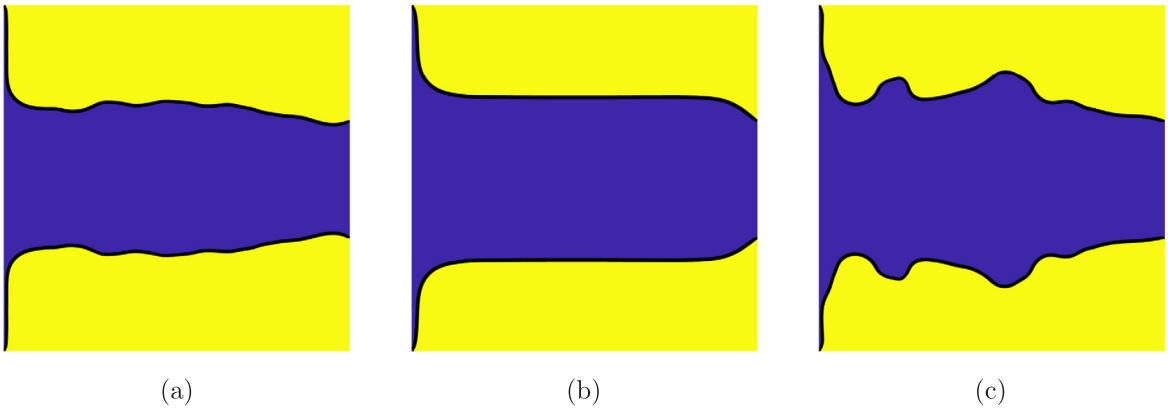

Fig. 8. The optimal designs obtained with different external force terms. (a)–(c) are the results with the external force terms are $[-150, 0]$, $[0,\ 0]$, and $[150,\ 0]$, respectively.

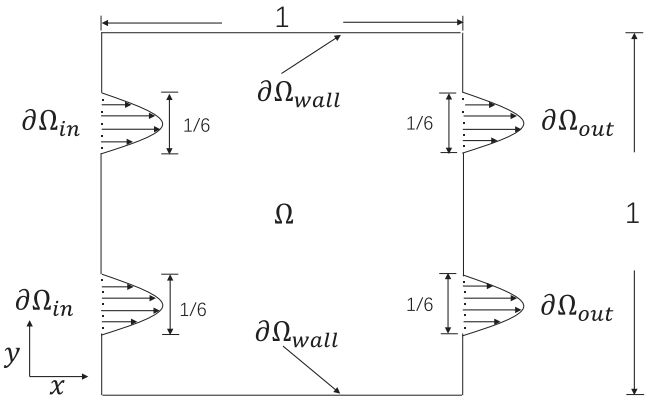

Fig. 9. Schematic illustration of the initial condition.

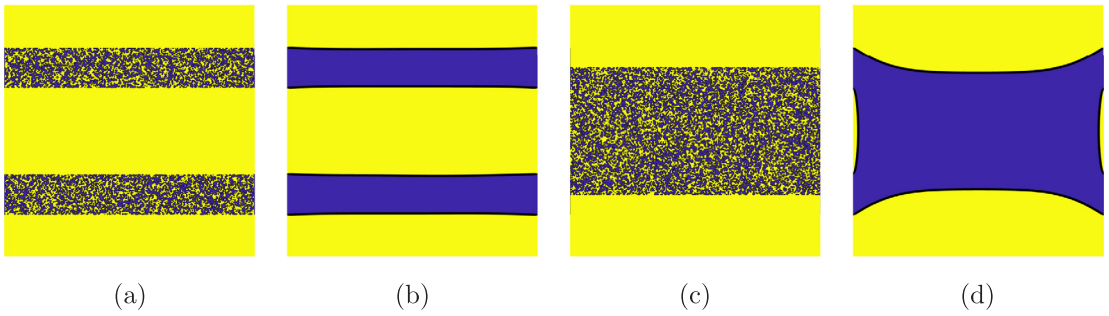

Fig. 10. (b) and (d) are the final results of initial configurations of (a) and (c), respectively.

respectively. Two different initial configurations are described as in Fig. 10(a) and (c). Fig. 10(b) and (d) are the optimal configurations of Fig. 10(a) and (c), respectively. Obviously the different locations of inflow/outflow can lead to different optimal designs.

4.8. Effect of volume constraints

To verify effect of volume constraints on the optimal design, we consider the bend pipe design problem in Fig. 11(a). We set $\overline{g} = 1$ and $\beta = 500$. The centers of inflow and outflow are located in $[0, 3/4]$ and $[3/4, 0]$. The other parameter

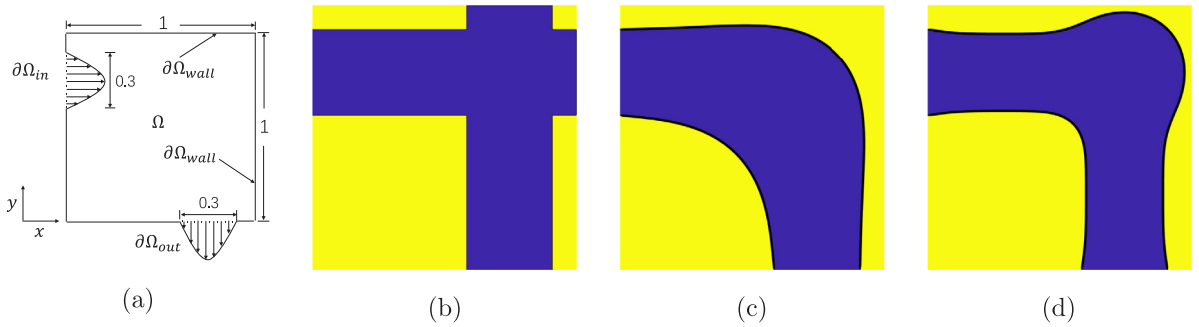

Fig. 11. (a) Schematic illustration of the inflow and outflow. (b), (c), and (d) are evolution of the phase field. (b) Initial shape. (c) Result with volume constraint. (d) Result without volume constraint.

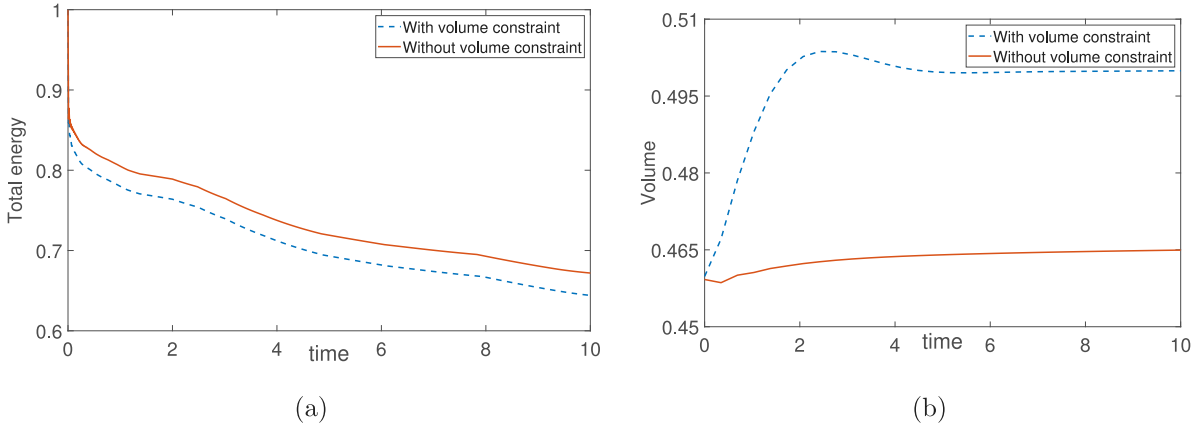

Fig. 12. Comparison between the evolution of total energy (a) and evolution of volume $A(\phi)$ (b) with and without volume constraints.

values are $\gamma = 10$ and $V_0 = 0.5$. The experiment with or without volume constraint is performed until $T = 10$. The results are shown as in Fig. 11. As can be seen, compared with the case with constraint, the thickness of the pipe wall without constraint obviously increases. Fig. 12 indicates the evolution curves basically coincide with each other.

4.9. Effect of the inlet and outlet size

The size of inlet and outlet plays a great role in simulation of blood flowing in blood vessels [64,65]. Here, the design domain is $\Omega = (0, 2) \times (0, 1)$ with a mesh grid 256×128. We set $\overline{g} = 1$, $\beta = 5000$, $\gamma = 10$, and $V_0 = 0.55$. The diameter of inlet is 0.3 and the diameter of outlet is 0.6. The locations of inlet and outlet are shown in Fig. 13(a). The corresponding centers are located in $[0, 0.25]$, $[0, 0.75]$ and $[1, 0.5]$. Fig. 13(b)–(d) show the evolved flow shapes at different times. In order to investigate the effect of the diameter of the inlet and outlet, we compare three experiments in Figs. 14 and 15. We find that the results obtained are indeed affected by the diameter of outlet and inlet.

4.10. Effect of the fixed solid structures

Now, we investigate how solid structures affect the fluid optimal designs. The solid structure is expressed by ψ. Analogously to the previous example in Section 4.2, we choose the same default parameter values. The schematic of the initial and boundary conditions are the same as Fig. 13(a), however, the diameters of inlet and outlet are set to be 1 and 0.3, respectively. A series of numerical simulations with varying solid structures are performed in this Section. Here, varying solid structures are achieved by placing different numbers of solid balls in different positions in the same diffuser as shown in the first row of Fig. 16. The evolution results are summarized in the second row of Fig. 16. We observe that solid structures affect the optimal results obviously.

4.11. Optimization of a 3D diffuser

As the final example for topology optimization in fluid, a 3D diffuser is considered as shown in Fig. 17(a). The domain is $\Omega = (0, 1) \times (0, 1) \times (0, 1)$ with a $100 \times 100 \times 100$ mesh grid. Here, we set three flow profiles on the inflow boundary

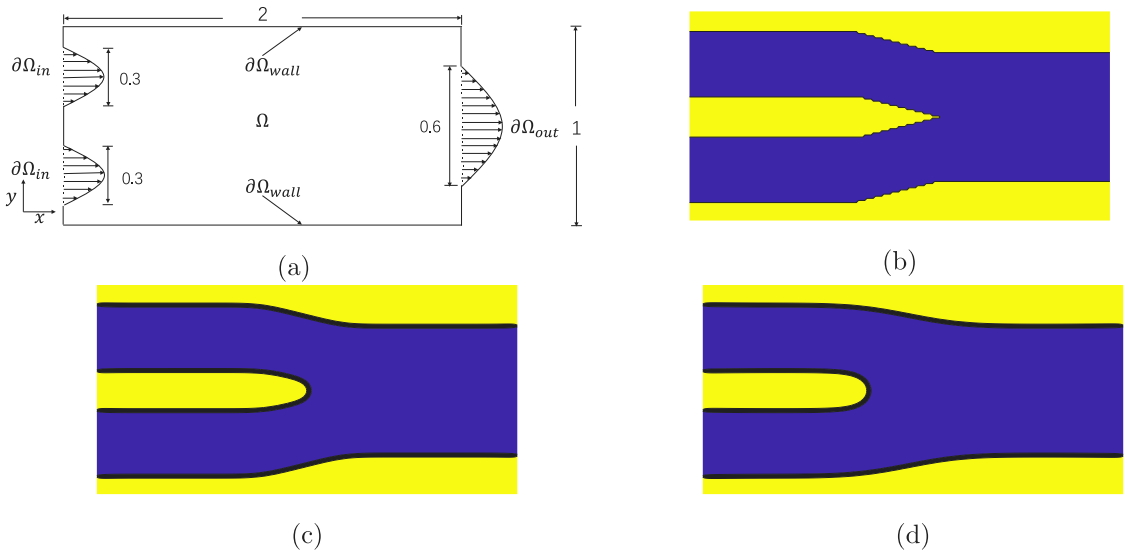

Fig. 13. (a) Schematic of the configuration for inflow and outflow. (b), (c), and (d) are evolutions of the flow in porous medium at time $t = 0, 0.5,$ and 1.5, respectively.

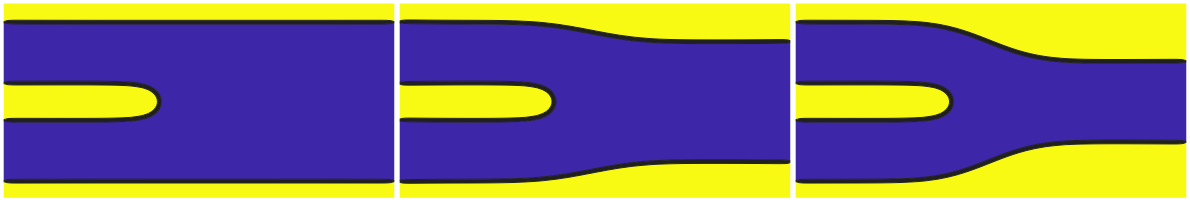

Fig. 14. The effect of outlet diameters on the optimal configuration for the flow. From left to right, the diameters of outlet are 0.8, 0.6, and 0.4, respectively. The diameter of inlet is fixed as 0.6.

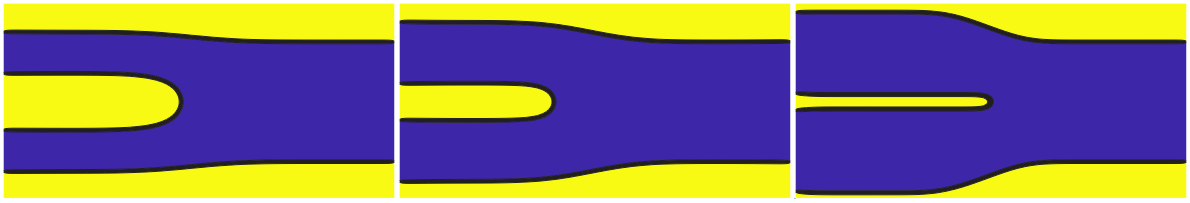

Fig. 15. The effect of inlet diameters on the optimal configuration for the flow. From left to right, the diameters of inlet are 0.8, 0.6, and 0.4, respectively. The diameter of outlet is fixed as 0.6.

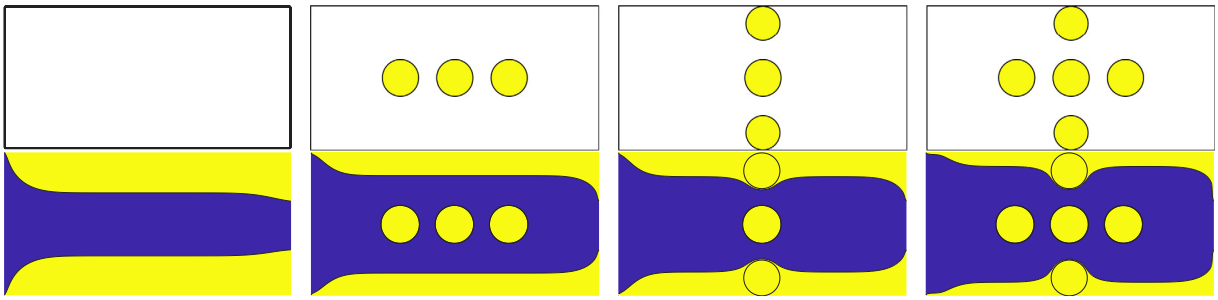

Fig. 16. Evolution of the phase field. Top: Initial configurations with different solid structures. Bottom: The optimal results corresponding to different initial configurations.

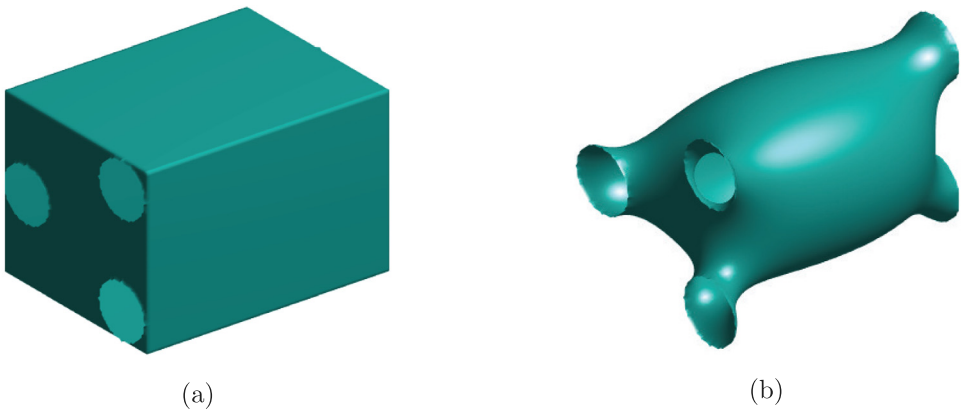

Fig. 17. The initial configuration of 3D diffuser (a) and the optimal result (b) by our scheme.

with centers of circles being (1/4, 1/2), (3/4, 1/4) and (3/4, 3/4) on the plane of $x = 0$. We set two flow profiles on the outflow boundary with centers of circles being (1/2, 1/4) and (1/2, 3/4) on the plane of $x = 1$. Note that the radius of all circles equals 0.24. We set $\overline{g} = 2$ and $\overline{g} = 3$ for the three inflow profiles and the two outflow profiles, respectively. $V_0 = 0.5$ is used and other parameter settings are the same as for the previous 2D problems in Section 4.2. It can be seen from Fig. 17 that the optimal configuration obtained is relatively smooth and clear after 100 iterations, which indicates that our proposed scheme can be applied to solve the three-dimensional optimization problem.

5. Conclusion

In this paper, we presented first- and second-order unconditionally energy stable schemes for fluid-based topology optimization problems. Using a porous media approach, our objective functional composed of five terms including mechanical property, Ginzburg–Landau energy, two penalized terms for solid, and the volume constraint. We coupled the Stokes type equation and the Allen–Cahn equation to obtain the evolved equation for fluid-based topology optimization. We used the backward Euler method and the Crank–Nicolson method to discretize the coupling system. The first- and second-order accurate schemes were presented for the system. The proof of unconditional stabilities for our proposed schemes was given. For the numerical solutions, we used the preconditioned conjugate gradient method to solve the system. Several numerical tests were performed to verify the efficiency and accuracy of our proposed schemes. There have been quite a few existing works of convergence analysis and error estimate for the phase field model coupled with fluid motion, such as convergence analysis of a fully discrete finite difference scheme for Cahn–Hilliard–Hele–Shaw equation [66], error analysis of a mixed finite element method for a Cahn–Hilliard–Hele–Shaw system [67]. In the future, we will consider the convergence analysis and error estimate for the fluid-based topology optimization problem. It is well known that the original Allen–Cahn equation satisfies the maximum principle. While it is difficult to prove that Eq. (2.19) satisfies the maximum principle or not. Recently, a class of maximum principle preserving schemes were studied for the generalized Allen–Cahn equation [59,61]. In the future, we will consider a maximum principle preserving and energy stable scheme for fluid-based topology optimization problem.

Declaration of competing interest

The authors declare that they have no known competing financial interests or personal relationships that could have appeared to influence the work reported in this paper.

Acknowledgment

Y.B. Li is supported by the Fundamental Research Funds for the Central Universities, China (No. XTR042019005). The corresponding author (J.S. Kim) was supported by Korea University Grant, Republic of Korea. The authors are grateful to the reviewers whose valuable suggestions and comments significantly improved the quality of this paper.

References

[1] Dugast F, Favennec Y, Josset C, Fan Y, Luo L. Topology optimization of thermal fluid flows with an adjoint Lattice Boltzmann Method. J Comput Phys 2018;365(15):376–404.
[2] Norgaard S, Sigmund O, Lazarov B. Topology optimization of unsteady flow problems using thelattice Boltzmann method. J Comput Phys 2016;307:291–307.
[3] Jenkins NW, Maute K. An immersed boundary approach for shape and topology optimization of stationary fluid–structure interaction problems. Struct Multidiscip Optim 2016;54(5):1191–208.
[4] Munk DJ, Kipouros T, Vio GA, Steven GP, Parks GT. Topology optimisation of micro fluidic mixers considering fluid–structure interactions with a coupled Lattice Boltzmann algorithm. J Comput Phys 2017;349(15):11–32.
[5] Pingen G, Maute K. Optimal design for non-Newtonian flows using a topology optimization approach. Comput Math Appl 2010;59(7):2340–50.
[6] Sato A, Yamada T, Izui K, Nishiwaki S, Takata S. A topology optimization method in rarefied gas flow problems using the Boltzmann equation. J Comput Phys 2019;395:60–84.
[7] Gersborghansen A, Sigmund O, Haber RB. Topology optimization of channel flow problems. Struct Multidiscip Optim 2005;30(3):181–92.
[8] Yaji K, Yamada T, Yoshino M, Matsumoto T, Izui K, Nishiwaki S. Topology optimization in thermal-fluid flow using the lattice Boltzmann method. J Comput Phys 2016;307:355–77.
[9] Yu Q, Wang K, Xia B, Li Y. First and second order unconditionally energy stable schemes for topology optimization based on phase field method. Appl Math Comput 2021;405:126267.
[10] Zhang W, Xiao Z, Liu C, Mei Y, Youn SK, Guo X. A scaled boundary finite element based explicit topology optimization approach for three-dimensional structures. Internat J Numer Methods Engrg 2020;121(21):4878–900.
[11] Zhou M, Lian H, Sigmund O, Aage N. Shape morphing and topology optimization of fluid channels by explicit boundary tracking. Internat J Numer Methods Fluids 2018;88(6):296–313.
[12] Kreissl S, Maute K. Levelset based fluid topology optimization using the extended finite element method. Struct Multidiscip Optim 2012;46:311–26.
[13] Coffin P, Maute K. A level–set method for steady-state and transient natural convection problems. Struct Multidiscip Optim 2016;53(5):1047–67.
[14] Villanueva CH, Maute K. CutFEM topology optimization of 3D laminar incompressible flow problems. Comput Methods Appl Mech Engrg 2017;444–73.
[15] Feppon F, Allaire G, Bordeu F, Cortial J, Dapogny C. Shape optimization of a coupled thermal fluid–structure problem in a level set mesh evolution framework. SeMA J 2019;76:413–58.
[16] Lundgaard C, Alexandersen J, Zhou M, Andreasen CS, Sigmund O. Revisiting density-based topology optimization for fluid–structure-interaction problems. Struct Multidiscip Optim 2018;58(3):969–95.
[17] Allaire G, Dapogny C, Delgado G, Michailidis G. Multi-phase structural optimization via a level set method. ESAIM: COCV 2014;20(2):576–611.
[18] Koch JRL, Papoutsiskiachagias EM, Giannakoglou KC. Transition from adjoint level set topology to shape optimization for 2D fluid mechanics. Comput Fluids 2017;150:123–38.
[19] Yonekura K, Kanno Y. Topology optimization method for interior flow based on transient information of the lattice Boltzmann method with a level-set function. JPN J Ind Appl Math 2017;34(2):611–32.
[20] Dugast F, Favennec Y, Josset C. Reactive fluid flow topology optimization with the multi-relaxation time lattice Boltzmann method and a level-set function. J Comput Phys 2020;409:109252.
[21] Shen C, Hou L, Zhang E, Lin J. Topology optimization of three-phase interpolation models in Darcy–Stokes flow. Struct Multidiscip Optim 2018;57(4):1663–77.
[22] Nogueira X, Ramirez L, Khelladi S, Chassaing JC, Colominas I. A high-order density-based finite volume method for the computation of all-speed flows. Comput Methods Appl Mech Engrg 2016;298(1):229–51.
[23] Wu S, Hu X, Zhu S. A multi-mesh finite element method for phase-field based photonic band structure optimization. J Comput Phys 2018;257:324–37.
[24] Yang X. Linear, first and second-order, unconditionally energy stable numerical schemes for the phase field model of homopolymer blends. J Comput Phys 2016;327:294–316.
[25] Duan X, Li F, Qin X. Topology optimization of incompressible Navier–Stokes problem by level set based adaptive mesh method. Comput Math Appl 2016;72(4):1131–41.
[26] Coffin P, Maute K. Level set topology optimization of cooling and heating devices using a simplified convection model. Struct Multidiscip Optim 2016;53:985–1003.
[27] Li F, Hu X. A phase-field method for shape optimization of incompressible flows. Comput Math Appl 2019;77(4):1029–41.
[28] Gomez H, Nogueira X. An unconditionally energy-stable method for the phase field crystal equation. Comput Methods Appl Mech Engrg 2013;249–252(1):52–61.
[29] Ranirez L, Nogueira X, Khelladib S, Chassaing JC, Colominas I. A new higher-order finite volume method based on moving least squares for the resolution of the incompressible Navier–Stokes equations on unstructured grids. Comput Methods Appl Mech Engrg 2014;278(15):883–901.
[30] Guillen-Gonzalez F, Tierra G. Unconditionally energy stable numerical schemes for phase-field vesicle membrane model. J Comput Phys 2018;354(1):67–85.
[31] Guillen-Gonzalez F, Rodriguez-Bellido MA, Tierra G. Linear unconditional energy-stable splitting schemes for a phase-field model for nematicisotropic flows with anchoring effects. Internat J Numer Methods Engrg 2016;108:535–67.
[32] Chen H, Wang X. A one-domain approach for modeling and simulation of free fluid over a porous medium. J Comput Phys 2014;259:650–71.
[33] Chen W, Conde S, Wang C, Wang X, Wise SM. A linear energy stable scheme for a thin film model without slope selection. J Sci Comput 2012;52(3):546–62.
[34] Li W, Chen W, Wang C, Yan Y, He R. A second order energy stable linear scheme for a thin film model without slope selection. J Sci Comput 2018;76(3):1905–37.
[35] Cheng K, Qiao Z, Wang C. A third order exponential time differencing numerical scheme for no-slope-selection epitaxial thinfilm model with energy stability. J Sci Comput 2019;81(1):154–85.
[36] Yang J, Kim J. An unconditionally stable second-order accurate method for systems of cahn–hilliard equations. Commun Nonlinear Sci Numer Simul 2020;87:105276.
[37] Yu Q, Wang K, Xia B, Li Y. First and second order unconditionally energy stable schemes for topology optimization based on phase field method. Appl Math Comput 2021;405:126267.
[38] Olesen LH, Okkels F, Bruus H. A high-level programming-language implementation of topology optimization applied to steady-state Navier–Stokes flow. Internat J Numer Methods Engrg 2006;65(7):975–1001.
[39] Borrvall T, Petersson J. Topology optimization of fluids in Stokes flow. Int J Numer Methods Fluids 2003;41:77–107.

[40] Dede L, Garcke H, Lam KF. A Hele–Shaw–Cahn–Hilliard model for incompressible two-phase flows with different densities. J Math Fluid Mech 2018;20:531–67.
[41] Barrett JW, Garcke H, Nurnberg R. A stable numerical method for the dynamics of fluidic membranes. Numer Math 2016;134:783–822.
[42] Hintermuller M, Hinze M, Kahle C. A goal-oriented dual-weighted adaptive finite element approach for the optimal control of a nonsmooth Cahn–Hilliard–Navier–Stokes system. Optim Eng 2018;19:629–62.
[43] Evans LC, Gariepy RF. Measure theory and fine properties of functions. Math. chem. ser., Boca Raton, FL: CRC Press; 1992.
[44] Li Y, Kim J. Multiphase image segmentation using a phase-field model. Comput Math Appl 2011;62(2):737–45.
[45] Li Y, Guo S. Triply periodic minimal surface using a modified Allen—Cahn equation. Appl Math Comput 2017;295:84–94.
[46] Li Y, Jeong D, Choi J-I, Lee S, Kim J. Fast local image inpainting based on the Allen–Cahn model. Digit Signal Process 2015;37:65–74.
[47] Li Y, Lee D, Lee C, Lee J, Lee S, Kim J, Ahn S, Kim J. Surface embedding narrow volume reconstruction from unorganized points. Comput Vis Image Underst 2014;121:100–7.
[48] Li Y, Kim J. Fast and efficient narrow volume reconstruction from scattered data. Pattern Recognit 2015;48(12):4057–69.
[49] Li H, Li Y, Yu R, Sun J, Kim J. Surface reconstruction from unorganized points with L0 gradient minimization. Comput Vis Image Underst 2018;169:108–18.
[50] Li Y, Lan S, Liu X, Lu B, Wang L. An efficient volume repairing method by using a modified Allen–Cahn equation. Pattern Recognit 2020;107:107478.
[51] Li Y, Xia Q, Yoon S, Lee C, Lu B, Kim J. Simple and efficient volume merging method for triply periodic minimal structures. Comput Phys Comm 2021;264:107956.
[52] Garcke H, Hecht C. Applying a phase field approach for shape optimization of a stationary Navier–Stokes flow. ESAIM: Control Optim Calc Var 2016;22:309–37.
[53] Garcke H, Hinze M, Kahle C, Lam KF. A phase field approach to shape optimization in Navier–Stokes flow with integral state constraints. Adv Comput Math 2018;44:1345–83.
[54] Miyakawa T. On uniqueness of steady Navier–Stokes flows in an exterior domain. Adv Math Sci Appl 1995;5:411–20.
[55] Galdi GP, Sohr H. Existence and uniqueness of time-periodic physically reasonable Navier–Stokes flow past a body. Arch Ration Mech Anal 2004;172:363–406.
[56] Baeumle E, Ruzicka M. Note on the existence theory for evolution equations with pseudomonotone operators. Ric Mat 2017;66:35–50.
[57] Galdi GP. An introduction to the mathematical theory of the Navier–Stokes equations. New York: Springer; 2011.
[58] Zhao J, Yang X, Shen J, Wang Q. A decoupled energy stable scheme for a hydrodynamic phase field model of mixtures of nematic liquid crystals andviscous fluids. J Comput Phys 2016;305:539–56.
[59] Du Q, Ju L, Li X, Qiao Z. Maximum principle preserving exponential time differencing schemes for the nonlocal Allen–Cahn equations. SIAM J Numer Anal 2019;57:875–98.
[60] Shen J, Yang X. Numerical approximations of Allen–Cahn and Cahn–Hilliard equations. Discrete Contin Dyn Syst 2010;28(4):1669–91.
[61] Shen J, Tang T, Yang J. On the maximum principle preserving schemes for the generalized Allen–Cahn equation. Commun Math Sci 2016;14:1517–34.
[62] Li Y, Lee H, Jeong D, Kim J. An unconditionally stable hybrid numerical method for solving the Allen–Cahn equation. Comput Math Appl 2010;60:1591–606.
[63] Li Y, Jeong D, Kim H, Kim J. Comparison study on the different dynamics between the Allen–Cahn and the Cahn–Hilliard equations. Comput Math Appl 2019;77:311–22.
[64] Hyun J, Wang S, Yang S. Topology optimization of the shear thinning non-Newtonian fluidic systems for minimizing wall shear stress. Comput Math Appl 2014;67(5):1154–70.
[65] Zhang B, Liu X. Topology optimization study of arterial bypass configurations using the level set method. Struct Multidiscip Optim 2015;51(3):773–98.
[66] Chen W, Liu Y, Wang C, Wise SM. Convergence analysis of a fully discrete finite difference scheme for the Cahn–Hilliard–Hele–Shaw equation. Math Comp 2015;85(301):2231–57.
[67] Liu Y, Chen W, Wang C, Wise SM. Error analysis of a mixed finite element method for a Cahn–Hilliard–Hele–Shaw system. Numer Math 2017;135(3):1–31.